

# Investigating the role of mergers in galaxy assembly in the early Universe ( $z > 5$ )

A.Calabrò<sup>1</sup>, L.Pentericci<sup>1</sup>, M.Llerena<sup>1</sup>, S.Rossi<sup>2,1</sup>, L.Napolitano<sup>1</sup>, D.Bevacqua<sup>1</sup>, M.Giavalisco<sup>3</sup>, R.Somerville<sup>4</sup>, G.Gandolfi<sup>1</sup>, E.Daddi<sup>5</sup>, M.Dickinson<sup>6</sup>, S.Finkelstein<sup>7</sup>, A.Fontana<sup>1</sup>, M.Hirschmann<sup>8</sup>, J.S.Kartaltepe<sup>9</sup>, D.Kocevski<sup>10</sup>, A.Koekemoer<sup>11</sup>, H.Leung<sup>12</sup>, R.A.Lucas<sup>11</sup>, A.Taylor<sup>7</sup>, R.Tripodi<sup>1</sup>, X.Wang<sup>13,14,15</sup>, and L. Y. A. Yung<sup>11</sup>

<sup>1</sup> INAF - Osservatorio Astronomico di Roma, via Frascati 33, 00078, Monte Porzio Catone, Italy (antonello.calabro@inaf.it)

<sup>2</sup> Dipartimento di Fisica, Sapienza, Università di Roma, Piazzale Aldo Moro 5, 00185, Roma, Italy

<sup>3</sup> University of Massachusetts Amherst, 710 North Pleasant Street, Amherst, MA 01003-9305, USA

<sup>4</sup> Center for Computational Astrophysics, Flatiron Institute, 162 5th Avenue, New York, NY 10010, USA

<sup>5</sup> Université Paris-Saclay, Université Paris Cité, CEA, CNRS, AIM, 91191, Gif-sur-Yvette, France

<sup>6</sup> NSF's National Optical-Infrared Astronomy Research Laboratory, 950 N. Cherry Ave., Tucson, AZ 85719, USA

<sup>7</sup> The University of Texas at Austin, 2515 Speedway Blvd Stop C1400, Austin, TX 78712, USA

<sup>8</sup> Institute of Physics, Laboratory of Galaxy Evolution, Ecole Polytechnique Fédérale de Lausanne (EPFL), Observatoire de Sauverny, 1290 Versoix, Switzerland

<sup>9</sup> Laboratory for Multiwavelength Astrophysics, School of Physics and Astronomy, Rochester Institute of Technology, 84 Lomb Memorial Drive, Rochester, NY 14623, USA

<sup>10</sup> Department of Physics and Astronomy, Colby College, Waterville, ME 04901, USA

<sup>11</sup> Space Telescope Science Institute, 3700 San Martin Drive, Baltimore, MD 21218, USA

<sup>12</sup> SUPA, Institute for Astronomy, University of Edinburgh, Royal Observatory, Edinburgh EH9 3HJ, UK

<sup>13</sup> School of Astronomy and Space Science, University of Chinese Academy of Sciences (UCAS), Beijing 100049, China

<sup>14</sup> National Astronomical Observatories, Chinese Academy of Sciences, Beijing 100101, China

<sup>15</sup> Institute for Frontiers in Astronomy and Astrophysics, Beijing Normal University, Beijing 102206, China

## ABSTRACT

Galaxy mergers play a crucial role in shaping the morphology, the star formation, and the mass growth of galaxies across cosmic time. While mergers have been extensively investigated in the local Universe, the evolution of their frequency and physical properties in the early Universe has yet to be fully understood. In this work, we investigate the role of mergers in a large spectroscopic sample of 1233 galaxies in the range  $5 < z < 14$  with good detection ( $S/N_{\text{pixel}} > 3$ ) in the JWST/F444W band, covering six different extragalactic fields (COSMOS, UDS, GOODS-South, GOODS-North, EGS, and Abell2744). We identify mergers from rest-frame optical disturbances in F444W, using a combination of Gini,  $M_{20}$ , and Asymmetry morphological parameters, which trace more advanced mergers (including also minor mergers) with shorter observability timescales compared to the close photometric pair selection. We find a morphological merger fraction  $f_m$  that does not strongly evolve with redshift from  $z = 0$  to  $z \sim 8$ . The average  $f_m$  of our primary major merger condition ( $\text{Gini}+0.14 \times M_{20} \geq 0.33$ ,  $A \geq 0.35$ ) is  $\sim 5\%$ , which increases to an average  $f_m$  of  $\sim 8\%$  for longer merger observability tracers and to  $f_m$  of  $\sim 13\%$  for major+minor merger tracers. Accounting for the evolving merger timescale of each tracer, we find that the merger rate is strongly increasing from  $z = 1$  to  $z = 7$  by more than one order of magnitude, averaging  $\sim 2$  merger/galaxy/Gyr at redshifts  $5 < z < 10$  for major mergers (in agreement with photometric pair studies), and a factor of  $\sim 3$  higher for minor+major mergers. We finally perform SED modeling using available HST+JWST photometry to infer stellar masses and SFRs (averaged over multiple timescales), using a non parametric star-formation history. We find that mergers at this cosmic epoch have a significant impact, although significantly lower than at  $z < 1$ , on the star-formation rate (SFR) of galaxies. When averaged over  $\leq 10$  Myr (comparable to the observability timescale of morphological disturbances at  $z > 5$ ), their SFRs are a factor of  $\sim 1.7$  higher than a mass and redshift matched sample of non-mergers, suggesting that mergers trigger new star-formation through short-lived powerful bursty episodes. Despite this, mergers contribute only by 5%-10% to the mass build-up of galaxies in the redshift range explored, suggesting that in-situ star-formation is the dominant process in galaxy growth at all cosmic epochs.

**Key words.** galaxies: evolution — galaxies: high-redshift — galaxies: formation — galaxies: interactions — galaxies: star-formation — galaxies: statistics

## 1. Introduction

Galaxy mergers play a fundamental role in the evolution of galaxies over cosmic time. In  $\Lambda$ -CDM cosmology, they are a key mechanism for hierarchical structure formation, through which small dark matter halos and their host galaxies merge together to form larger halos, larger galaxy structures and more massive galaxies (Kormendy & Kennicutt 2004; Hopkins et al. 2008). Mergers also drive profound modifications of galaxies' mor-

phologies, as they are key channels for the conversion of spiral galaxies into elliptical and lenticular ones (Toomre & Toomre 1972; Barnes 1992; Naab et al. 2014). In the low redshift Universe, they also impact the star-formation rate (SFR) of the galaxies. In the SDSS survey, Patton et al. (2013) found a SFR enhancement of a factor of  $\sim 2.5$  in mergers compared to isolated systems at  $z \approx 0$ . Using HST images, a similar result was found in close pairs with projected separations of  $< 5$  kpc by

Shah et al. (2022) at  $z = 1$ , while at higher redshifts ( $1 < z < 3$ ) the SFR enhancement decreases to a factor of  $\times 1.5$ . In contrast, Pearson et al. (2019b) do not find any significant enhancement of the SFR in mergers compared to isolated galaxies in a sample of 200k galaxies at  $0 < z < 4$ .

Recently, JWST has revolutionized the study of galaxy morphology and mergers in the early Universe ( $z > 5$ ) by providing near-infrared images with unprecedented depth and resolution, revealing details in the rest-frame UV and optical (e.g., faint interacting features, double nuclei) that were not accessible with other space-based and ground-based facilities. This has allowed us to identify sizable samples of mergers during the reionization epoch (EoR), thus exploring the relevance of mergers and their impact on the SFR during the first Billion year of cosmic time.

Different approaches can be used to identify mergers. The first, simpler approach relies on selecting galaxy pairs that are close on the sky (up to a maximum separation) and with consistent photometric redshifts (e.g., Mundy et al. 2017, Duncan et al. 2019). Using this approach on recent JWST observations, several works have found that the merger rate at  $z > 5$  is orders of magnitude higher than in the local Universe Duan et al. (2025); Puskás et al. (2025a). According to Duan et al. (2025), mergers also play an important role in the galaxy mass accretion at that epoch, contributing  $\sim 50\%$  to the mass build-up of galaxies, comparable to the mass accretion from star formation. However, this result is not confirmed by other studies, with Puskás et al. (2025a) finding a much lower merger contribution of  $\sim 10\%$ .

The impact of mergers on the SFR at the EoR is also a hotly debated issue. Puskás et al. (2025b), based on  $\sim 2000$  galaxies in the JADES survey at redshifts 3-9, find that photometric pairs with projected separations  $< 20$  kpc have a specific SFR (sSFR) enhancement by a factor of  $1.12 \pm 0.05$  compared to isolated galaxies at the same stellar mass ( $M_*$ ) and redshift. Although this effect is smaller at high- $z$  compared to the local Universe, mergers still have a significant impact on the SFR at  $z > 3$ . In contrast, Duan et al. (2026) found no statistical enhancement in sSFR for close pairs at any projected separation at  $z > 5$ .

Despite the relative simplicity of the close pair approach, it presents several limitations. First, it mainly traces the early phases of galaxy interactions rather than advanced mergers, hence providing a limited and incomplete picture of the merger phenomenon. Since it does not rely on the detection of galaxy distortions or asymmetries, the true interacting nature of the system and its final fate crucially depend on the accuracy of photometric redshifts and on the relative velocity of the two galaxies.

Alternative approaches are able to select mergers in more advanced phases of the interaction. These include the visual inspection of the galaxy morphology, which has been successfully adopted for morphological classification in the CANDELS fields with HST images (Kartaltepe et al. 2015), and more recently applied also on JWST observations of galaxies in the CEERS survey up to  $z \sim 9$  (Kartaltepe et al. 2023). However, the main limitations of this approach are reproducibility and feasibility for large samples of galaxies. In order to solve these limitations, machine learning techniques have also been adopted in the last decade for merger selection (e.g., Huertas-Company et al. 2015, 2018; Pearson et al. 2019a; Margalef-Bentabol et al. 2024; Ferreira et al. 2020). However, the final classification crucially depends on the dataset that is used for training the algorithm. Even though hydrodynamical simulations can also be adopted to define the ground truth on the merger nature of a system, projects based on this approach have shown contrasting results, with accuracies of the final merger selection ranging from 40% to  $\sim 75\%$  (Guzmán-Ortega et al. 2023; Rose et al. 2023).

Another approach that is feasible for large samples is based on the measurement of some fundamental morphological parameters, namely Asymmetry (A), Gini, and  $M_{20}$ , which were introduced by Conselice et al. (2003) and Lotz et al. (2004) to identify mergers from HST images of galaxies at  $z < 3$ . These parameters are highly sensitive to the presence of a disturbed and asymmetric structure, features due to interactions such as connecting bridges and tidal tails, shells, and double nuclei embedded in a common, more diffused gaseous and stellar envelopes. They are thus well suited to identify evolved, pre-coalescence, merger stages, complementary to the close pair selection. Recently, they have been successfully adopted in several works to identify morphological disturbances in galaxies from JWST images (e.g., Liang et al. 2024; Polletta et al. 2024; Westcott et al. 2025). This quantitative morphological analysis has also been adopted by Dalmasso et al. (2024) to study the fraction and properties of mergers in a sample of 675 photometrically selected galaxies at  $4 < z < 9$  in the background of the Abell2744 cluster field. They find no significant redshift dependence of the merger fraction, and no significant difference in the sSFR between merging and non-merging galaxies. However, their sample could still be contaminated by low-redshift interlopers, which could potentially have a significant impact both on the merger rate and on their average properties, especially at the highest redshifts where the statistics are very poor.

In this paper, we expand on the study of Dalmasso et al. (2024), revisiting the role of mergers in galaxy mass assembly and determining to what extent mergers affect star formation during the reionization epoch. Compared to this previous work, we complement the non parametric morphology approach with a visual inspection to increase the purity of the merger selection. We also improve the statistics by considering all the CANDELS fields, namely GOODS-North, GOODS-South, UDS, EGS, and COSMOS. Moreover, given the larger number of spectroscopic confirmations and observations that are now publicly available from JWST, we select galaxies spectroscopically in order to avoid contamination from low-redshift interlopers, while retaining a good sample of statistics for a robust analysis. Despite this stricter requirement, we extend the analysed sample of Dalmasso et al. (2024) by a factor of  $\sim 2$ . The availability of spectroscopic data also allows us to study the emission line properties and ionizing source of merging galaxies, which will be investigated in a subsequent work.

Our paper is organised as follows. In Section 2, we present our spectroscopic sample selection and our methodology to assess galaxy morphologies. We also describe the SED fitting procedure through which we derive fundamental galaxy parameters, including stellar masses and SFRs. In Section 3, we present our results on the merger fraction evolution at  $z > 5$  and on the SFR enhancement in mergers versus isolated galaxies. In Section 4, we discuss our results and compare them to predictions of semi-analytic models and simulations. Finally, we present a summary and conclusions in Section 5.

Throughout the paper, we adopt the AB magnitude system Oke & Gunn (1983), we assume a flat  $\Lambda$ CDM cosmology with  $\Omega_m = 0.3$ ,  $\Omega_\Lambda = 0.7$ , and  $H_0 = 70 \text{ km s}^{-1} \text{ Mpc}^{-1}$ , and a Chabrier (2003) initial mass function (IMF). We use the Astropy package (Astropy Collaboration et al. 2022), the photutils package (Bradley 2023)<sup>1</sup>, and the statmorph python package (Rodríguez-Gomez et al. 2019; Rodríguez-Gomez 2019) for the calculation of morphological parameters.

<sup>1</sup> <https://photutils.readthedocs.io/en/stable/citation.html>

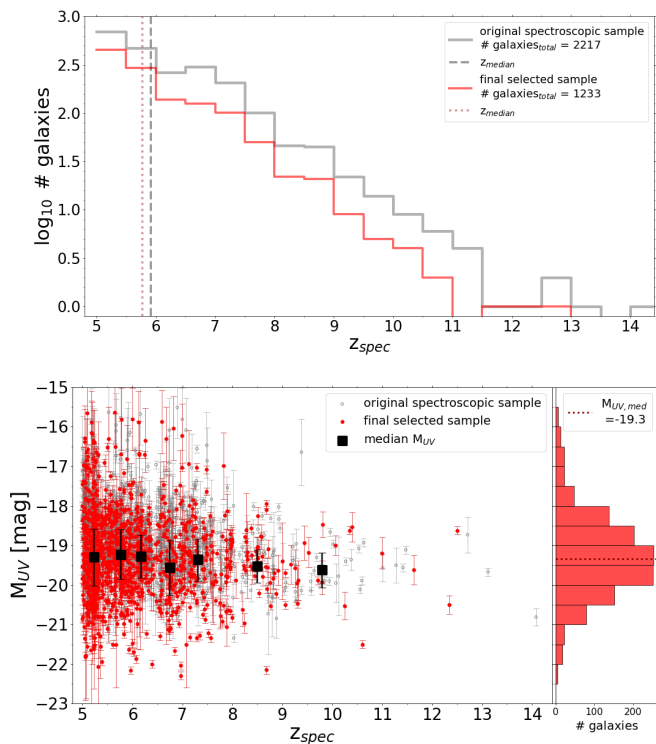


**Fig. 1.** *Top:* Histogram of the redshift distribution of the original spectroscopic sample selected from DJA with  $z_{\text{spec}} > 3$  (gray line) and of the final selected sample after applying the  $S/N_{\text{pixel}}$  cut (red line). *Bottom:* Scatter plot highlighting the  $M_{\text{UV}}$  distribution as a function of redshift for the original spectroscopic sample and the final sample (gray and red circles, respectively). The median values of  $M_{\text{UV}}$  in increasing redshift bins are highlighted with black squares. The histogram of  $M_{\text{UV}}$  for the selected sample is also shown on the y right axis, with the median  $M_{\text{UV}}$  indicated by a horizontal dashed line.

## 2. Methodology

### 2.1. Spectroscopic sample selection

The galaxy sample analyzed in this work is drawn from the DAWN JWST Archive (DJA<sup>2</sup>), which is an online public repository including the most recent JWST data products. In particular, we considered the latest version (v4.4) of the DJA spectroscopic catalog (DJA-Spec, Valentino et al. 2025,<sup>3</sup>), which includes spectroscopic observations and best-fit spectroscopic redshifts obtained from the Early Release Science (ERS) surveys to the most recent surveys performed in Cycle 3 with public data, such as CAPERS. We included the data taken in six different fields, including EGS, GOODS-SOUTH, GOODS-NORTH, UDS, and COSMOS, which were originally part of the CANDELS fields (Grogin et al. 2011; Koekemoer et al. 2011), with the addition of the field covering the background of the galaxy cluster Abell2744, which was part of the Hubble Frontier Fields (Lotz et al. 2014; Coe et al. 2015). The main advantage of these fields is that they were the first targets of JWST imaging and spectroscopic observations. The spectra were taken by several surveys during the last three years, the largest of which include CEERS (ERS-1345; Finkelstein et al. 2023, 2025), GLASS (ERS-1324 and DDT-2756; Treu et al. 2022; Mascia et al. 2024), JADES (GTO-1180, 1210, GO-3215; Bunker et al. 2024; Eisenstein et

al. 2025), UNCOVER (GO-2561; Bezanson et al. 2024), RUBIES (GO-4233, De Graaff et al. 2025), and CAPERS (GO-6368). In these fields, deep, multiwavelength JWST imaging is also available from the same surveys.

The spectra assembled in DJA were reduced with the GRIZLI (Brammer 2023) and MSAExp (Brammer 2023; Heintz et al. 2025) software, following a uniform spectroscopic reduction procedure that is described in detail in Heintz et al. (2023) and de Graaff et al. (2024). The v4 release delivers to the community merged FITS files including all the 1D ‘optimally’ extracted spectra available from different NIRSpec gratings and from the PRISM. We performed a photometric correction to the spectra using the photometry available in the ASTRODEEP-JWST multi-band photometric catalog of Merlin et al. (2024). However, as already outlined in Heintz et al. (2025), the 1D spectra retrieved from DJA already show an overall consistency within 10-15% with the photometric data.

As a preliminary selection, we considered galaxies in the DJA-Spec catalog in the six fields listed above and with a robust (quality flag = 3) spectroscopic redshift  $\geq 5$ , also confirmed through a visual inspection. This redshift limit was chosen because it represents approximately the redshift limit up to which mergers and merger fractions were estimated from previous HST surveys in the CANDELS fields (Kartaltepe et al. 2007; Duncan et al. 2019). This limit also allows us to compare our findings to similar JWST studies performed at the same redshifts, and based on the photometric close pair method (e.g., Puskás et al. 2025a; Duan et al. 2025). With these criteria, we obtained an initial sample of 2217 galaxies. The redshift distribution of this sample is presented in Fig. 1-top (gray line), and shows that the number of sources decreases exponentially from  $z = 5$  to  $z = 14$ , with a median redshift  $z_{\text{med}} \simeq 6$ . Lastly, we used the galaxy spectra to derive the UV magnitudes  $M_{\text{UV}}$  at 1500 Å rest-frame, using the methodology outlined in Dottorini et al. (2025). We find  $M_{\text{UV}}$  ranging between  $-22.5$  and  $-15.5$  (Fig. 1-bottom), with median  $M_{\text{UV}}$  values that are not significantly evolving with redshift.

### 2.2. Derivation of morphological parameters from NIRCам images

We derive the morphological parameters of the galaxies from  $2.5'' \times 2.5''$  cutouts<sup>4</sup> in the NIRCам F444W band. The main motivation of this choice is that F444W traces the optical rest-frame for almost the entire redshift range spanned by our sample, thus the galaxy structure and merger identification are more directly comparable to lower redshift studies (at  $z < 3$ ) based on the HST/F160W band. We note, however, that the spatial resolution of JWST at  $4.4\mu\text{m}$  is better than the one of HST at  $1.6\mu\text{m}$ , allowing us to detect finer and smaller galaxy structures. Bluer NIRCам bands, despite the higher resolution, mainly trace the rest-frame UV emission in our redshift range, which might be more affected by inhomogeneous dust distribution and might not trace real interacting features or merger driven asymmetric structure (Calabrò et al. 2019; Cibinel et al. 2019).

The morphological parameters selected for the merger identification are the Gini, the  $M_{20}$ , and the asymmetry parameters. We calculate them through *statmorph*, a python package for the quantitative assessment of galaxy structure, and which is mostly based on the code written in IDL by Lotz et al. 2004 and Lotz et al. 2008a. The definitions of these parameters are based on the original works of Conselice et al. (2003) and Lotz et al. (2004),

<sup>2</sup> <https://dawn-cph.github.io/dja/blog/2025/05/01/nirspec-merged-table-v4/>

<sup>3</sup> [doi:10.5281/zenodo.15472354](https://doi.org/10.5281/zenodo.15472354)

<sup>4</sup> We download the cutouts using the grizli cutout service: <https://grizli-cutout.herokuapp.com/>

and recently reported in our previous studies (Treu et al. 2023; Dalmasso et al. 2024). However, we describe them in the Appendix A for completeness.

An important step of the morphological analysis is the visual inspection of the cutout and removal of low redshift interlopers that wrongly fall in the same segmentation map of the main central galaxy. This is done through the comparison of the original segmentation maps derived with our procedure to the photometric catalog of Merlin et al. (2024). In case of a system with two clearly separated galaxies belonging to the same segmentation map, we checked whether the photometric redshift (or the spectroscopic one, if available) of the offset component is consistent with the spectroscopic redshift of the central galaxy. In case of inconsistent redshifts, we remove the secondary galaxy from the segmentation map through a deblending procedure and rerun the morphological parameters routine.

Finally, for each galaxy, we also estimate the average S/N per pixel ( $S/N_{\text{pixel}}$ ) within its segmentation map, which we will use to assess the accuracy and reliability of the morphology calculations, as we explain in the following section.

### 2.3. Reliability of morphological parameters

When observing galaxies at increasing redshifts, we have to consider that their structural appearance might be significantly altered because of surface brightness dimming, which roughly scales with redshift as  $(1+z)^{-4}$  (e.g., Whitney et al. 2020). This could potentially bias the estimation of morphological parameters. We note that in those extreme cases when the galaxies have a very low surface brightness and the signal-to-noise of the images is very low, STATMORPH produces an error in the calculation, hence these cases can be easily discarded. In general, the effect of cosmological dimming, S/N and image resolution on the morphological parameters has been extensively investigated at different redshifts and for a variety of surveys (e.g., Lotz et al. 2011; Petty et al. 2014; Whitney et al. 2021; Westcott et al. 2025; Sazonova et al. 2025). Due to the different effects of the complications listed above, it is worth discussing the effects on asymmetry separately from the effects on Gini and  $M_{20}$ .

According to Lotz et al. (2004), the rotational asymmetry, which requires image subtractions and corrections for the background noise signal, becomes less robust at low  $S/N_{\text{pixel}}$ . This parameter is also affected by the degradation of the image resolution, even though this effect is not as significant as the dependence on signal-to-noise (Thorp et al. 2021). In particular, the asymmetry tends to be underestimated both at low  $S/N_{\text{pixel}}$  and low effective resolution (i.e., the number of resolution elements sampling the galaxy, Bottrell et al. 2019, Thorp et al. 2021, Sazonova et al. 2024). However, Lotz et al. (2011) found that by setting a lower limit on the  $S/N_{\text{pixel}} \geq 2$  in HST F160W images of galaxies at  $z \leq 2$ , the asymmetry is robust and not affected by systematic biases. Similarly, Conselice & Arnold (2009) find that asymmetry measurements are accurate also at higher redshifts (between 2 and 6), hence they do not apply any corrections to their measured values. More recent simulations by Sazonova et al. (2025) have shown that at  $S/N_{\text{pixel}} \geq 3$  and with the F444W resolution, the underestimation is relatively small with a maximum bias of 0.05. Finally, Westcott et al. (2025) have performed a series of simulations to test the effect of surface brightness dimming on the measurement of morphological parameters of galaxies at  $z > 5$  using JWST mock images. They estimated the morphological parameters of the galaxies at their photometric redshifts (with a similar procedure to the one adopted in this paper) and compared the results to those obtained when artificially

redshifting the galaxies to a higher redshift. Their main finding is that the asymmetry does not differ significantly when the galaxies are simulated at higher redshifts, provided that the signal-to-noise is sufficiently high. In particular, at redshift  $z > 8$ , it might be slightly underestimated by 2.5% on average.

On the other hand, Gini and  $M_{20}$  are more robust against decreasing S/N compared to the asymmetry parameter A, changing less than 10% ( $\Delta < 0.05$  and  $< 0.2$ ) for an average  $S/N_{\text{pixel}} > 2$  at spatial resolution better than 1000 pc and 500 pc (respectively) per resolution element (Lotz et al. 2004). Their reliability down to average  $S/N_{\text{pixel}} \geq 2$  has been independently confirmed by other works (i.e., Holwerda et al. 2011; Lisker 2008; Sazonova et al. 2025; Petty et al. 2014; Yao et al. 2023; Salvador et al. 2024). These parameters are instead more sensitive to decreasing spatial resolution. In particular, the former is slightly underestimated at low resolution, while the latter can be overestimated. However, both are stable when the segmentation map of the detected source is covered by a sufficient number of resolution elements (approximately  $> 10$ ), which is always satisfied by the mergers in our sample in F444W, as we mostly trace pre-coalescence systems with a more extended structure than isolated galaxies by definition. Secondly, we use a combination of Gini and  $M_{20}$ . Since  $\text{Gini}+0.14 \times M_{20}$  measures the perpendicular distance in the G- $M_{20}$  plane, the resolution dependencies of the two parameters mostly cancel out, resulting in a stable measurement for all the galaxies with good  $S/N_{\text{pixel}}$ .

Overall, previous studies consistently showed that above a minimum spatial resolution, the  $S/N_{\text{pixel}}$  can be used to discriminate between reliable and unreliable morphological parameters estimations, hence to select galaxy samples with more robust structural properties. There might still be a slight underestimation of the asymmetry parameter, but we prefer not to apply any corrections to the measured values as they would be very uncertain and highly inaccurate (being derived from simulations). With this choice, it will also be easier to compare our analysis to other works (both at lower and similar redshifts) using the standard asymmetry definition and merger threshold (e.g. Conselice et al. 2009; Dalmasso et al. 2024; Westcott et al. 2025).

### 2.4. Final sample selection

We follow a similar approach to the studies presented above, and require a minimum  $S/N_{\text{pixel}}$  of 3 for our sample, slightly more conservative than in Lotz et al. (2004) and Lotz et al. (2011). We have verified that this choice works better at isolating problematic fits than applying a simple cut based on the S/N of the total photometry of the galaxy as done in Dalmasso et al. (2024). In particular, this condition removes all the measurements where statmorph yields unphysical, negative asymmetries. At the same time, this criterion allows us to retain a larger number of galaxies for the analysis, significantly improving the statistics. With this condition, we obtain a final sample of 1233 galaxies,  $\sim 56\%$  of the initial sample. Their redshift distribution is shown in Fig. 1 (red line). Despite this further selection, the shape of the distribution, the redshift limits ( $5 < z < 14$ ), and the median redshift of the final sample ( $z_{\text{median}} = 6.0$ ), are similar to those of the original spectroscopic sample.

In Fig. 1-bottom we show the distribution of  $M_{\text{UV}}$  of our final sample as a function of redshift. Similarly as above, the distribution of  $M_{\text{UV}}$  is not significantly different between the original sample and the final selected one, implying that the  $S/N_{\text{pixel}}$  cut in F444W does not introduce systematic biases on  $M_{\text{UV}}$ . The median  $M_{\text{UV}}$  of the final sample is  $-19.3$ , and it is not a strong function of redshift. Our final sample is on average 1

magnitude fainter than the sample of [Dalmaso et al. \(2024\)](#), due to their very strict requirements on the total photometric S/N of the sources ( $S/N_{\text{total}} > 7$ ) and on their apparent magnitude ( $m_{AB} < 28.87$ ), hence we are more complete toward fainter objects. Notably, our  $M_{UV}$  distribution is similar to the entire DJA spectroscopic catalog from [Heintz et al. \(2025\)](#). Our sample is instead shifted toward brighter magnitudes on average compared to purely photometric JWST samples in the literature. For example, considering the photometric catalog of [Endsley et al. \(2024\)](#) in JADES, one of the deepest JWST imaging surveys, our galaxies are brighter in  $M_{UV}$  by approximately 0.6 magnitudes at  $z = 6$ . We have also checked that  $M_{UV}$  does not show a correlation with  $S/N_{\text{pixel}}$ . In particular, galaxies with  $S/N_{\text{pixel}}$  lower and higher than 3 do not have significantly different  $M_{UV}$  distributions, as the  $M_{UV}$  does not take into account the redshift of the source and its physical size. For this reason,  $M_{UV}$  is not as effective as the  $S/N_{\text{pixel}}$  to isolate problematic fits of the morphological parameters.

## 2.5. Derivation of stellar masses and SFRs from SED fitting

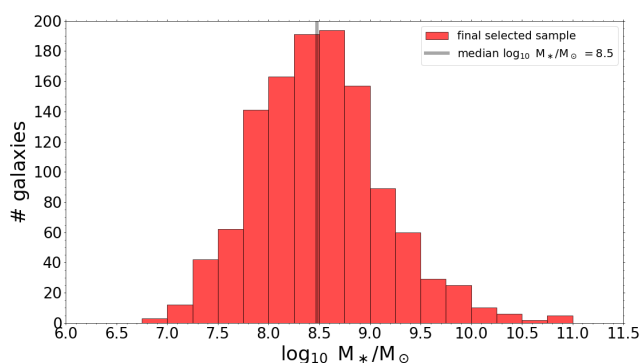


**Fig. 2.** Histogram of the stellar mass distribution of the final selected, spectroscopic sample. The median stellar mass of the sample is highlighted with a vertical black shaded line.

We derived two fundamental galaxy properties, namely the stellar mass and the SFR, from an SED fitting procedure using the available photometric data covering the rest-frame UV and optical of the galaxies, following the methodology of [Llerena et al. \(2025\)](#). In brief, we adopted the ASTRODEEP-JWST photometric catalog of [Merlin et al. \(2024\)](#), which includes NIR-Cam+HST multiband total photometry covering all the five extragalactic deep fields considered in this work, and spanning the wavelength range between 0.4 and 4.4  $\mu\text{m}$ . This range includes the following 16 filters in order of wavelength: F435W, F606W, F775W, F814W, F090W, F105W, F115W, F125W, F140W, F150W, F160W, F200W, F277W, F356W, F410M, and F444W. The object detection is made with SExtractor v2.8.6 on a weighted F444W+F356W image, and total photometry is derived in each photometric band with the A-PHOT software ([Merlin et al. 2019](#)), with a setup that is optimized for the faint and extended objects found in the high redshift Universe.

We fitted the photometry with BAGPIPES (version 1.2.0, [Carnall et al. 2018](#)), adopting [Gutkin et al. \(2016\)](#) stellar population templates, and fixing the redshift to the spectroscopic value. We adopted a non-parametric SFH as in [Leja et al. \(2019\)](#), according to which a constant SFR is fit in seven bins of increasing lookback times. In the first four bins, the SFR is calculated within the following ranges: 0–3, 3–10, 10–30, and 30–100 Myr, while the last four bins are logarithmically spaced between 100 Myr and the maximum allowed age (corresponding to  $z = 20$ ).

The stellar metallicity was free to vary in the range 0.01–0.5  $Z_{\odot}$ . We adopted a [Calzetti et al. \(2000\)](#) attenuation law with  $A_V$  ranging from 0 to 2 magnitudes. Finally, a nebular component was included based on CLOUDY photoionization models ([Ferland et al. 2017](#)), and the ionization parameter  $\log(U)$  was free to vary between  $-4$  and 0. The IGM attenuation is modeled according to [Inoue et al. \(2014\)](#).

For the scope of our current project, deriving the SFRs from the photometry presents two main advantages compared to line based estimates. First, most of the spectra are taken with the NIRSpec-MSA configuration, whose slitlets ( $0.2'' \times 0.46''$ ) might trace only a small portion of the galaxies and are thus not representative of the whole systems, especially in the presence of merger features and extended interacting components. Even calibrating the spectra with the available photometry, the line based properties rely on the assumption that the gaseous emission has the same spatial distribution as the stellar continuum emission, which might not hold for all the galaxies. Using the total photometry for the estimation of physical properties allows us to minimize these biases. Secondly, our SED fitting procedure allows us to compute SFRs averaged over timescales of 3 Myr, 10 Myr, 30 Myr, and 100 Myr. As shown by [Llerena et al. \(2024\)](#), the SFRs averaged over the last 10 Myrs agree well with those derived from optical recombination lines. Using the different timescale estimates, we can define a burstiness parameter as the ratio of a short timescale SFR over the 100 Myr averaged SFR, as  $SFR_{t_{\text{short}}}/SFR_{100\text{Myr}}$ , where  $t_{\text{short}}$  varies between 3 Myr and 10 Myr. We will use this parameter in Section 3.4.

The stellar masses of our sample range between  $\log_{10} M_*/M_{\odot} = 7$  and 11, with a median value of 8.5 ( $1\sigma = 0.6$ ), as shown in Fig. 2. This is  $\sim 0.6$  dex higher than the median stellar mass that can be reached by JWST with a purely photometric selection, such as the one performed by [Duan et al. \(2025\)](#), suggesting that our spectroscopic selection and the  $S/N_{\text{pixel}}$  threshold trace on average more massive galaxies compared to a photometrically selected sample at the same cosmic epoch. We will further analyse the SFRs in Section 3.3.

## 2.6. Merger identification

We use the morphological parameters introduced in Section 2.2 to classify galaxies as mergers and non-mergers. We follow a similar approach to our previous work in [Dalmaso et al. \(2024\)](#). This is a combination of the merger classification criteria adopted in [Lotz et al. \(2004\)](#) and [Conselice et al. \(2003\)](#), which are based, respectively, on the Gini and  $M_{20}$  parameters, and on the asymmetry. We thus classify a galaxy as a merger when both the two following conditions are satisfied :

$$\begin{aligned} A &\geq 0.35 \\ G + 0.14 \times M_{20} &> 0.33 \end{aligned} \quad (1)$$

This corresponds to the gold sample criterion defined in [Dalmaso et al. \(2024\)](#), and represents our primary merger selection. Combining the two conditions maximizes the robustness of the merger selection. These limits have been validated at  $z > 5$  in [Dalmaso et al. \(2024\)](#), and are based on the evidence that the intrinsic morphological parameters of mergers and normal isolated galaxies do not significantly evolve with redshift on average ([Treu et al. 2023](#); [Vulcani et al. 2023](#)), allowing us to use the same thresholds that are adopted in the original studies at  $z \leq 3$ . We can visualize the distribution of the Asymmetry, Gini, and  $M_{20}$  parameters of our sample in Fig. 3, where the two conditions in Equation 1 are highlighted with green lines and divide

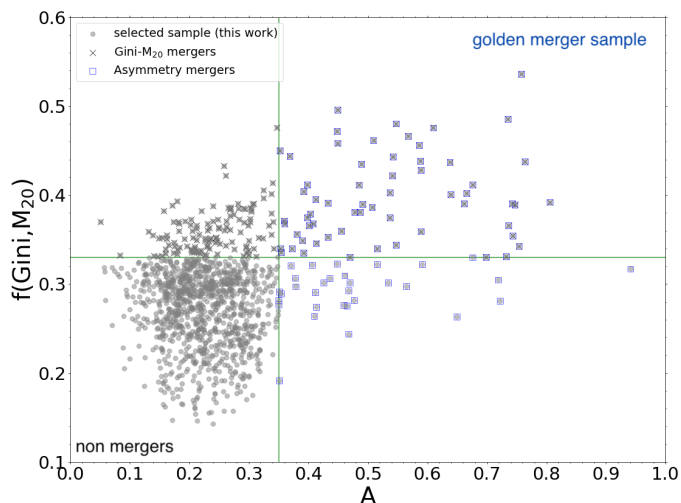


**Fig. 3.** Diagram of the Asymmetry vs  $f(\text{Gini}, M_{20})$  for our selected sample, where  $f(\text{Gini}, M_{20}) = \text{Gini} + 0.14 \times M_{20}$ . The two merger criteria defined in Equation 1 are shown with a vertical and horizontal green line. Non merger galaxies are highlighted with simple gray circles. On top of them, we show a black cross for Gini- $M_{20}$  mergers and a blue empty square for asymmetry mergers.

the scatter plot in four parts. We find that 80 galaxies are classified as mergers according to both conditions, occupying the top right quarter in Fig. 3.

We additionally consider two merger subsets, dubbed the asymmetry and the Gini- $M_{20}$  mergers, which are identified by applying respectively the first and second condition of Equation 1. We create these additional samples as we think that they likely probe different merger types and different merger observability timescales, as we will explain in the following section. We find in total 92 galaxies satisfying the  $A > 0.35$  condition, while 186 galaxies fall in the category of Gini- $M_{20}$  mergers. 1016 galaxies ( $\sim 80\%$  of the sample) are instead non-mergers. These classes of galaxies are highlighted with different symbols in Fig. 3.

We note that the merger criteria defined in Equation 1 based on morphological parameters select galaxies with major morphological disturbances and with bright off-centered components, which are the best candidates of ongoing mergers according to previous simulations (Conselice 2007; Lotz et al. 2011; Snyder et al. 2015, 2019). In this work, for our goals, we identify morphological disturbed galaxies as mergers, and use ‘merger candidate fraction’ as a synonym of ‘true merger fraction’.

This merger definition has some limitations. First,  $f(\text{Gini}, M_{20})$  and the asymmetry might not be enhanced (compared to normal isolated galaxies) during all phases of the interaction. Secondly, the amount of their enhancement depends on a variety of factors, including impact parameters, mass ratios, gas fractions, and spin of the colliding galaxies (e.g., Di Matteo et al. 2008). Moreover, they might not identify the majority of late stage interactions and post mergers because interacting features tend to rapidly fade after the coalescence (Lotz et al. 2008a, see also discussion in Pawlik et al. 2016).

Finally, we remark that our approach differs from the standard techniques based only on the analysis of morphological parameters, as we also perform a visual inspection (as discussed in Section 2.2) of the galaxies aimed at maximizing the purity of the merger sample. We show example galaxy cutouts for each of the four morphological classes defined by the criteria in Eq. 1 and represented in Fig. 3 in the appendix C in Fig. C.1.

## 2.7. Merger timescales

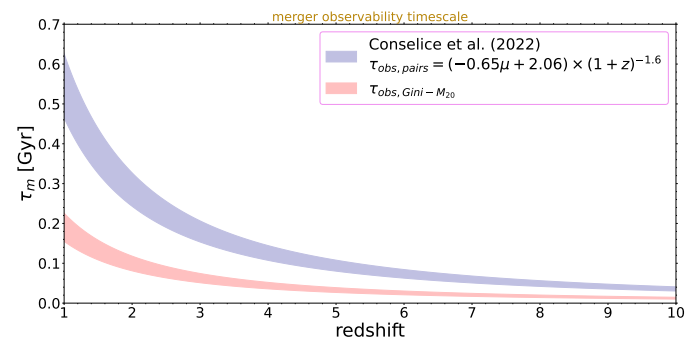


**Fig. 4.** Merger observability timescales  $\tau_m$  in the redshift range 0-10 that we assume in this work for the close pair method (from Conselice et al. 2022, shaded dark blue region) and for the golden merger sample (light blue region). The shaded region encompasses the  $\tau_{obs}$  expected for mass ratios  $\mu$  between 1 and 4.

In order to convert the observed merger fraction to a physical rate at which galaxies merge, it is essential to understand how the merger dynamical time evolves with cosmic time and what is the observability timescale probed by each specific tracer. The merger dynamical time  $\tau_m$  is the timescale by which two merging galaxies finally coalesce into a single nucleus. This timescale decreases with redshift, such that galaxies in the early Universe merge faster than those at lower redshifts (Snyder et al. 2017). An analytic function describing this redshift variation has been recently derived by Conselice et al. (2022), who used IllustrisTNG 300-1 simulations to study at different redshifts how long it takes at different redshifts for a close pair to finally merge. (see also Ferreira et al. 2020). They found that  $\tau_m$  also depends on the mass ratio  $\mu$  of the merging galaxies, such that major mergers (lower  $\mu$ ) are faster than minor mergers (higher  $\mu$ ). In particular, they derived the following expression for  $\tau_m$ , which assumes a projected pair separation of  $\sim 30$  kpc :

$$\tau_m(z) = a \times (1+z)^b, \quad (2)$$

where  $a = -0.65 \pm 0.08 \times \mu + 2.06 \pm 0.01$ , and  $b = -1.60 \pm 0.01$ . Slightly different parameters, with an exponent  $b = -2.0$  and  $a = 2.4$ , have been proposed by Snyder et al. (2017), but they yield results that are not significantly different than our assumed values from Conselice et al. (2022). The modeled evolution of the dynamical merger timescale is also similar to the typical halo dynamical timescale,  $0.1t_H(z)$ , where  $t_H(z)$  is the Hubble-time (i.e. age of the Universe) at redshift  $z$ . However, this assumption would yield slightly longer  $\tau_m$  at  $z < 1$  and shorter  $\tau_m$  at  $z > 1$  compared to the function in equation 2. We can see the  $\tau_m(z)$  produced by these models in Fig. 4.

We note that the merger timescale defined in Equation 2 depends on the maximum physical distance considered for the photometric pairs in the simulation. Selecting interacting pairs closer (wider) than 30kpc projected, we should consider shorter (longer) merger timescales. According to Lotz et al. (2011), assuming baryonic mass ratios  $> 4$  (i.e., major mergers), the close pair method at low redshifts ( $0 < z < 1$ ) traces  $\tau_m$  values of the order  $\sim 330$  Myr when adopting small projected separations of  $5 \text{ kpc } h^{-1} < R_{proj} < 20 \text{ kpc } h^{-1}$ , 600 Myr when choosing pairs with  $10 \text{ kpc } h^{-1} < R_{proj} < 30 \text{ kpc } h^{-1}$ , and  $\geq 1.5$  Gyr when choosing larger separations of  $\geq 100 \text{ kpc } h^{-1}$ .

If we consider mergers identified through their morphological properties, several studies at low redshifts ( $z < 2$ ) have

shown that different morphological parameters and merger conditions are sensitive to different phases of the merger process, typically shorter than the merger dynamical time defined above. This phenomenon can be parametrized by the merger observability timescale  $\tau_{obs}$ . However,  $\tau_{obs}$  of the method only plays a role if it is shorter than the intrinsic merger event timescale.

In detail, the Gini- $M_{20}$  condition is sensitive to minor and major mergers according to Lotz et al. (2011), probing mass ratios of the colliding galaxies between 1 : 1 and 10 : 1, over timescales of  $\sim 200$  Myr, independent of the mass ratio. This is indeed the phase when the two galactic nuclei are enclosed in a common envelope, thus they are more likely to be identified within the same segmentation map, increasing both Gini (because of unequal flux distribution) and  $M_{20}$  (because of bright off-centered structures).

The asymmetry condition  $A \geq 0.35$  is sensitive to major mergers, in the mass ratio range between 1 : 1 and 4 : 1, as mergers with lower mass ratios produce fainter and undetectable asymmetric features (Conselice et al. 2003; Conselice 2007; Lotz et al. 2011). In this case the observability timescale is more difficult to model as it is a strong function of the gas fraction and of the mass ratio of the colliding galaxies (Lotz et al. 2011). The strong dependence on  $f_{gas}$  arises because more gas-rich mergers are more likely to form strong tidal features and large scale disturbances, which also last longer than in gas poor mergers (Lotz et al. 2010). Previous studies have attempted to estimate  $\tau_{obs}$  related to an enhanced asymmetry parameter. According to Lotz et al. (2011), for  $f_{gas} = 0.4$  and  $\mu \approx 3:1$ , the merger timescale is similar to the one traced by the photometric pair method for separations  $\leq 30$  kpc (i.e.,  $\sim 600$  Myr). In the simulations presented by Conselice (2007), the  $A \geq 0.35$  condition is not satisfied over the full time of the merging process, but only for  $\sim 2/3$  of the merger duration, for a total observability time of 0.4 Gyr on average at  $z \approx 1$ . In both cases, this timescale is significantly longer compared to that traced by the Gini- $M_{20}$  condition. Because of this considerations, the asymmetry  $\tau_{obs}$  at  $z \sim 1$  is likely comprised between the Gini- $M_{20}$   $\tau_{obs}$  and the close pair one. If we combine the two criteria in Equation 1, we are thus tracing major mergers with observability timescales of  $\sim 200$  Myr at  $z \sim 1$ .

At higher redshifts, there are no specific studies on the evolution of the observability timescales. Therefore, we estimate them at  $z > 1$  using the following reasoning. For the Gini- $M_{20}$   $\tau_{obs}$ , we consider the merger timescale  $\tau_m(z)$  as described by equation 2, and we rescale it by a constant factor as  $\tau_{obs,Gini-M_{20}}(z,\mu) = \tau_m(z,\mu) \times C$ . The constant factor  $C$  is anchored to  $z \sim 1$  and is set to  $1/3$ , ensuring that  $\tau_{obs,Gini-M_{20}}(z=1,\mu) \approx 200$  Myr, in agreement with Lotz et al. (2011). In practice, we assume that, at all redshifts, the Gini- $M_{20}$  criterion traces merger timescales that are one third of that probed by the close pair method with 30 kpc separation. The final  $\tau_{obs,Gini-M_{20}}(z)$  can be seen in Fig. 4 for a range of  $\mu$  from 1 to 10 (typical of minor+major mergers), and it follows a similar decreasing trend as  $\tau_m(z)$ , with smaller timescales probed as we go to higher redshifts, ranging from  $\sim 30$  Myr at  $z = 5$  to  $\sim 10$  Myr at  $z = 10$ . A similar evolution of the merger timescale can be applied to the gold merger criterion, which thus probes major mergers with  $\tau_{obs} < 30$  Myr at  $z > 5$ . We emphasize that the estimation of this parameter is very uncertain. However, it is physically reasonable to assume that it cannot be larger than  $\tau_m(z)$  and than the typical  $\tau_{obs}$  of close pairs, which would set an upper limit of  $\sim 100$  Myr at  $z > 5$ .

Considering the asymmetry observability timescale, we should expect a milder decrease with redshift at  $z > 1$  compared

to the Gini- $M_{20}$   $\tau_{obs}$  because the increasing gas fraction of typical star-forming galaxies (Daddi et al. 2010) partially balances the shorter merger duration in the early Universe. Following the indications of previous studies at lower redshifts, it is reasonable to assume that  $\tau_{obs,A \geq 0.35}$  at  $z > 5$  is likely comprised between  $\tau_{obs}$  of the Gini- $M_{20}$  criterion and the close photometric pair method. However, given its strong dependence on the mass ratio and gas fraction, whose evolution at our cosmic epochs is also very uncertain, we do not attempt to derive any quantitative estimates of this timescale, and we do not use it for the calculation of merger rates in the following part of the paper.

### 3. Results

#### 3.1. Evolution of the merger fraction at $z > 5$

In this section we calculate the fraction of mergers in our sample, and investigate how it varies across our redshift range and how it depends on other galaxy properties. We define the merger fraction in 7 bins of increasing redshifts as:  $f_m = \#mergers_{z-bin} / \#galaxies_{z-bin}$ , with uncertainties estimated using the statistics of Gehrels et al. (1986). The redshift bins are defined as 5-5.5, 5.5-6, 6-6.5, 6.5-7, 7-8, 8-9, and 9-12, where the bins at higher redshifts are larger in order to retain a good statistics.

We perform this analysis for different morphological indicators and merger criteria. For the gold merger sample, we find that the merger fraction is approximately constant at redshifts  $5 < z < 8$  with a median  $f_m = 4.8\%$ . It decreases at earlier cosmic epochs ( $z > 8$ ), even though in the last bin, where we have poorer statistics,  $f_m$  is still consistent with the median value (Fig. 5- panel A). For the asymmetry mergers,  $f_m$  varies between  $\sim 8\%$  and  $5\%$  from redshift 5 to 8, with a median fraction of  $f_m = 7.4\%$ . It decreases at higher redshifts, even though the uncertainties are significantly higher (Fig. 5- panel B). Finally, for the Gini- $M_{20}$  mergers,  $f_m$  ranges between  $\sim 11\%$  and  $\sim 17\%$  at  $5 < z < 9$ , while at  $z > 9$  it drops to  $\sim 5\%$  (Fig. 5- panel D).

Overall, merger indicators based on morphological parameters suggest that the merger fraction, while increasing from  $z = 0$  to  $z = 1$ , remains approximately constant at earlier epochs across  $\sim 7$  Gyr of cosmic history, and then again decreasing at  $z > 8$ . We find slight differences in normalization among different methods. For major merger tracers, longer merger timescale indicators yield on average higher merger fractions than short timescale indicators. Similarly, at fixed observability timescale, minor merger indicators yield higher merger fractions than major merger ones. The slight decrease in the last two bins is affected by low number statistics and is not highly significant. We would need a larger sample to confirm this trend at  $z > 8$ . However, we note that a similar decreasing trend of  $f_m$  is also found with the photometric pair method, using studies based on larger (photometric) samples, corroborating this observed trend. We will further discuss the differences with other samples, including photometric studies, in the following section.

The merger process might also depend on the stellar mass of the galaxies involved. Given the large range of stellar masses spanned by our sample (from  $\sim 10^7$  to  $\sim 10^{10} M_\odot$ ), we test possible variations of the merger fraction as we choose different  $M_*$  lower limits for our dataset, similar to the approach of Conselice et al. (2003) and Conselice et al. (2009). In particular, we consider lower limits of  $10^8 M_\odot$  and  $10^9 M_\odot$ , as cutting at even higher masses significantly reduces the available statistics. As a result, we find a similar redshift trend in all the stellar mass regimes, with an approximately constant  $f_m$  across the different cosmic epochs, as observed for the global sample. Most impor-

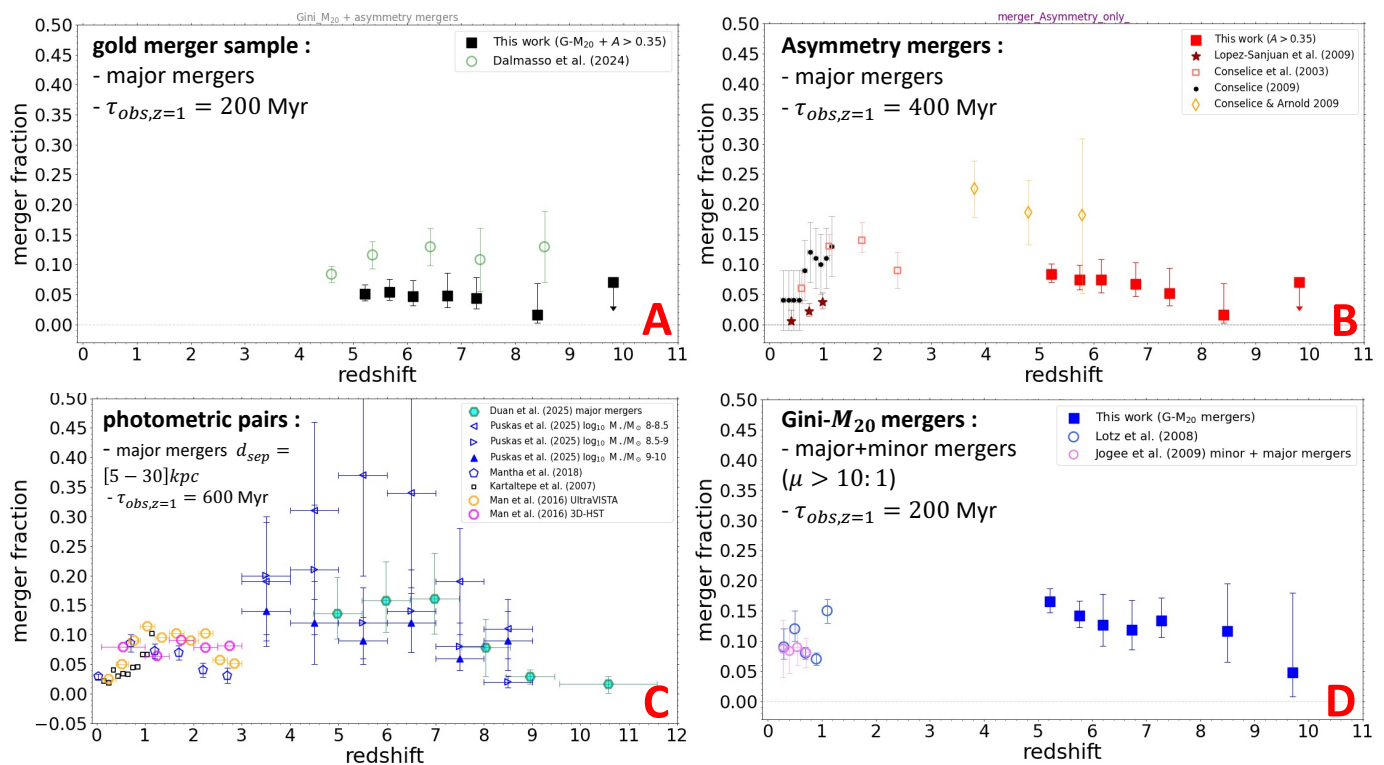


**Fig. 5.** Merger fraction  $f_m$  as a function of redshift for different merger identification methods : panel A) gold merger sample; panel B) asymmetry mergers ( $A \geq 0.35$ ); panel C) mergers identified through the photometric pairs; panel D) Gini- $M_{20}$  mergers. In each panel, our data is compared to several works in the literature at lower and similar redshifts adopting a similar merger identification technique.

tantly, we do not find any significant difference of the average merger fraction between the low mass and high mass galaxies in all the redshift bins. We summarize our findings in Table B.1 in the appendix B, where we specify the median stellar mass and the merger fraction in each redshift bin.

### 3.2. Comparison to other studies

It is interesting to compare our findings to previous works at lower and similar redshifts. The most direct comparison for the asymmetry sample is with the studies by López-Sanjuan et al. (2009), Conselice et al. (2003), Conselice et al. (2009), and Conselice & Arnold (2009), who adopt a morphological criterion which is identical to our one based on the asymmetry parameter (i.e.,  $A > 0.35$ ) to investigate mergers at  $z \leq 6$ . These studies indicate that there is a sudden increase of the merger fraction from the local Universe to  $z \simeq 0.5$ , with values ranging from  $\sim 3\%$  to  $\sim 15\%$  at  $z = 1$ . Afterwards, the merger fraction remains approximately constant up to the same cosmic epoch explored in this study, suggesting no strong evolution of  $f_m$  from  $z = 0.5$  to at least  $z = 8$  (Fig. 5-panel B). We must be aware that the low redshift studies are based in general on more massive samples compared to the galaxies analysed here, even though Conselice et al. (2003) did not find a significantly different trend of  $f_m$  as a function of stellar mass at  $z < 3$ . Lastly, we find a significantly lower merger fraction than Conselice & Arnold (2009) by a factor of  $\sim 2$ , which might be due to their study probing the rest-frame UV morphology of the galaxies at  $z > 3$ , which might be more asymmetric than the rest-frame optical. However, as mentioned in Section 1, part of the difference might also be due to sample selection, with their work probing more massive galaxies than our study.

For the Gini- $M_{20}$  mergers, we compare our results with similar studies performed at lower redshifts with HST images by Lotz et al. (2008b) and Jogee et al. (2009). Also with these diagnostics, we do not find a significant evolution of the merger fraction from  $z \sim 0.5$  to  $z \sim 9$ , with  $f_m$  ranging between 5% and 15% over that cosmic epoch (Fig. 5-panel D), even though low redshift studies are based in general on more massive galaxies than the ones analysed here.

There are no comparable studies at lower redshifts that consider the combination of the asymmetry and Gini- $M_{20}$  merger criteria. Therefore, we can only compare our golden merger sample to the results of Dalmasso et al. (2024). We find merger fractions that are systematically lower than in that work at the same redshift (Fig. 5- panel A). Presumably, this is due to the fact that no visual check and removal of low redshift companions was done in the previous analysis, leading to an overestimation of the true merger fraction.

For completeness, we also analyze the evolution of the merger fraction from the close pair method. In Fig. 5-panel C we plot the pair fractions ( $f_p$ ) obtained in several studies assuming a maximum projected distance separation of 30 kpc between the two galaxies. Previous HST based works in the CANDELS fields have constrained the pair fraction up to redshift  $\sim 3$ , finding an increase of  $f_m$  up to  $z \simeq 1$ , and a flattening from  $z = 1$  to  $z = 3$  around a value of 10%. However, as for the other low redshift studies, these works typically trace higher stellar masses of the primary galaxy ( $> 10^{10} M_\odot$ ) compared to our sample. Recently, JWST observations have allowed several works to measure  $f_p$  up to the reionization epoch and in a similar mass range to our selected sample, with stellar masses of  $> 10^8 M_\odot$  (Duan et al. 2025; Puskás et al. 2025a). They suggest that there is a slight increase of  $f_p$ , with peaks of 15%-30% around  $z \sim 6$  (depending

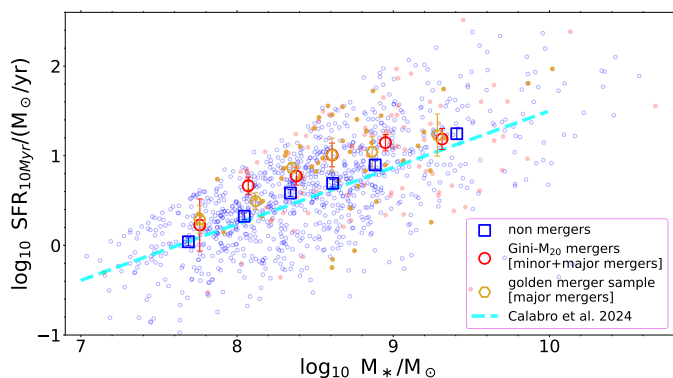


**Fig. 6.** Stellar mass vs SFR diagram for mergers versus non merger galaxies, in the redshift range  $5 < z < 8$ . The golden merger sample and the Gini- $M_{20}$  mergers, tracing respectively the major and major+minor mergers, are shown in small golden hexagons and red circles. The non-merger sample is shown with blue empty circles. Median SFRs (and uncertainties on the median) are calculated in six, equal populated redshift bins, and shown as bigger gold hexagons, red circles, and blue squares, respectively for the golden mergers, Gini- $M_{20}$  mergers, and non-mergers. The SFRs are averaged over 10 Myr, thus comparable to those inferred from the  $H\alpha$  line. The  $H\alpha$ -based Main Sequence of star-formation derived in Calabrò et al. (2024) in the CEERS and GLASS surveys is highlighted with a cyan dashed line.

on the study and on the mass range considered), which decreases again at  $z > 7$ .

We note that Puskás et al. (2025a) find a strong dependence of the pair fraction on stellar mass, with lower mass galaxies showing a higher  $f_p$  at fixed redshift. We remark that the pair fraction can be converted to a merger fraction by considering that a pair has a probability to merge into a single galaxy within  $1 \times \tau_{merge}$ . Assuming a probability of 100%, which is the typical assumption of those previous works,  $f_m = f_p$ . In this case, the major merger fraction based on photometric pairs follows a similar trend to the one based on morphology, with no strong evolution at redshifts  $\geq 1$ , even though it is systematically higher by a factor of  $\sim 2$ . Most of this discrepancy can be explained by the longer merger observability timescale probed by the close photometric pair compared to our morphological analysis. However, we note that assuming a lower merging probability for close pairs in previous studies (by  $\sim 50\%$ ) would also produce lower merger fractions that are in agreement with our work.

Overall, different merger indicators and selection techniques indicate that the fraction of mergers is not strongly evolving with redshift from  $z \approx 1$  to the epoch of reionization ( $z \approx 8$ ). We find instead different normalizations in the merger fraction vs redshift relations. This depends on the characteristic timescale of the merger diagnostic, with lower merger fractions found for shorter timescale indicators. In particular, our gold merger criterion yields merger fractions approximately a factor of 2 lower than the photometric pair selection. More abundant mergers are also found for minor+major merger tracers, such as the Gini- $M_{20}$  merger criterion, compared to major merger tracers.

### 3.3. Testing the SFR enhancement in merging galaxies

The main objective of the paper is to understand whether the merger process impacts the star-formation activity of early galaxies, as observed in the low redshift Universe. We perform this investigation primarily for the gold merger sample (top-right quadrant in Fig. 3), since they likely trace major mergers

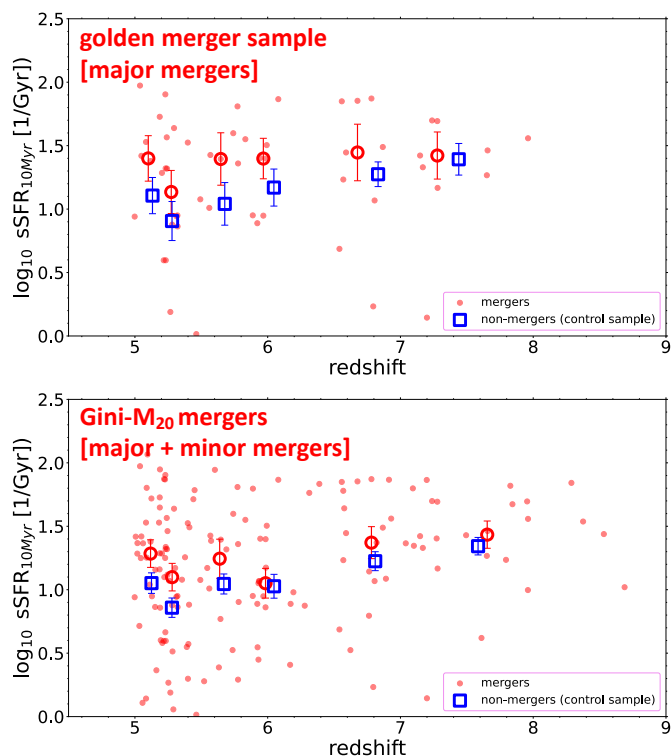


**Fig. 7.** Specific SFR (sSFR) vs redshift diagram for the golden merger sample and Gini- $M_{20}$  mergers (respectively in the upper and lower panel), compared to a mass and redshift matched sample of isolated galaxies, using a SFR timescales of 10 Myr.

over a short timescale, where we expect to have the strongest effects on galaxy properties, if there are any. Moreover, this is the most robust merger sample, as resulting from the combination of three different morphological parameters. However, for completeness, we will also explore the star-formation enhancement in the Gini- $M_{20}$  merger sample, as they likely probe a larger range of mass ratios (down to 10:1) with a similarly short observability timescale.

We first explore the stellar mass - SFR diagram. We limit the analysis to the redshift range 5-8, since the number of galaxies drops at  $z > 8$  resulting in poorer statistics (see Table B.1). Here we consider SFRs averaged over a timescale of 10 Myr, as they are comparable to those derived in other observational studies from recombination lines (e.g.,  $H\alpha$ ). Dividing our global sample in six equal populated stellar mass bins, we find a SFR vs  $M_*$  relation that is in agreement with the  $H\alpha$ -based star-forming Main Sequence (MS) derived by Calabrò et al. (2024) from star-forming galaxies at similar redshifts in the CEERS and GLASS surveys (Fig. 6). This comparison also suggests that our global sample does not have a significant bias compared to other JWST spectroscopic samples, in particular to the mass complete sample (down to an  $M_*$  limit of  $\log_{10}(M_*/M_\odot) = 7.8$  at  $z \sim 6$ ) analysed in Calabrò et al. (2024).

To test the effects of mergers on the SFR, we compare them to the non-merger sample, which is the one occupying the bottom-left quadrant in Fig. 3. While isolated galaxies agree well with the global MS relation, mergers show systematically higher SFRs in all the stellar mass bins, except the most massive one above  $\log_{10}(M_*/M_\odot) = 9.2$ , where the two subsets have similar median SFRs (Fig. 6). Considering the galaxies in the first 5 bins in the range of  $M_*$  between  $10^7$  and  $10^9 M_\odot$ , we find a SFR enhancement of  $0.25 \pm 0.04$  dex for both the golden and

the Gini- $M_{20}$  merger sample, that is, a factor of  $\sim 1.8$  higher compared to non-mergers. The different behaviour in the most massive bin could be due to timescale effects, or to different underlying physics. More massive mergers could be in a more advanced, post-coalescence merger stage, where the SFR has already reached its peak. Alternatively, more massive galaxies could experience dryer mergers (see [Lehnert et al. 2016](#)), or are subject to stronger feedback preventing new star-formation.

To investigate the redshift dependence of this enhancement, we analyze the cosmic evolution of the sSFR. In particular, we calculate the median sSFR in 6 equal-sized redshift bins for the merger subset and a control sample of non-mergers. This control sample was built by selecting for each merger a corresponding non-merging galaxy (randomly) with a similar stellar mass (within 0.2 dex) and a similar redshift (within 0.3). We show this comparison in Fig. 7 with a SFR averaged over the last 10 Myr. We find that mergers have a significant enhancement of sSFR compared to non-mergers across all redshift bins, with a median enhancement of  $0.22 \pm 0.04$  dex for the golden subset, not significantly evolving with redshift. The Gini- $M_{20}$  mergers have a slightly lower but still significant sSFR enhancement of  $0.17 \pm 0.04$  dex. The results shown in Fig. 6 and Fig. 7 for mergers and non-mergers are listed in Table B.2 in the appendix B.

Our findings are in line with [Puskás et al. \(2025b\)](#), who found a moderate sSFR enhancement in mergers (by  $\sim 10\%$ ) in JADES for galaxies with similar  $M_*$  and redshifts as this study, and using the smallest separation ( $\leq 20$  kpc) to identify close photometric pairs. We find a slightly higher enhancement than in their study, which might be due to our selection identifying more advanced merger phases where the two galaxies are more strongly interacting. In contrast, the non detection of a significant, merger-driven sSFR enhancement in [Duan et al. \(2025\)](#) and [Dalmaso et al. \(2024\)](#) might depend on a variety of factors, including sample selection. However, we note that our small effect would still be consistent with their  $3\sigma$  limits.

Finally, works at lower redshifts have investigated the merger induced SFR enhancement mainly in massive galaxies ( $M_* > 10^9 M_\odot$ ). For example, the most recent study from [Shah et al. \(2022\)](#) is representative of a more massive galaxy population (above  $10^{10} M_\odot$ ) at  $z = 0.5-3$ . While they find a significant SFR enhancement in mergers at  $z < 1.6$  by a factor of  $\sim 2.5$ , this effect almost vanishes in their higher redshift bin ( $1.6 < z < 3$ ), where they measure weaker enhancements of 1.23 and 1.06, respectively, for their merger sample and blended interactions sample, which are those more directly comparable to our selection. This suggests that in the early Universe the merger induced SFR enhancement is lower than at lower redshifts, at least for galaxies with masses  $> 10^9 M_\odot$  for which we can do this comparison.

### 3.4. Burstiness of merging vs isolated galaxies

Thanks to our SED fitting approach, we can investigate the SFR enhancement in mergers over different timescales in a quantitative way. This can also inform us on the SFH of merging galaxies compared to those that are forming stars in a steady-state or by gas accretion. In particular, we calculate for each galaxy the burstiness parameter defined before, comparing the SFR averaged over the last 3 Myr, 10 Myr, and 30 Myr, to the SFR averaged over 100 Myr. To perform a statistical analysis, we estimate for each timescale the median burstiness of the golden and Gini- $M_{20}$  merger subsets, taking into account the entire stellar mass and redshift range of our analysis, and then compare these results to the median burstiness obtained for a mass and redshift

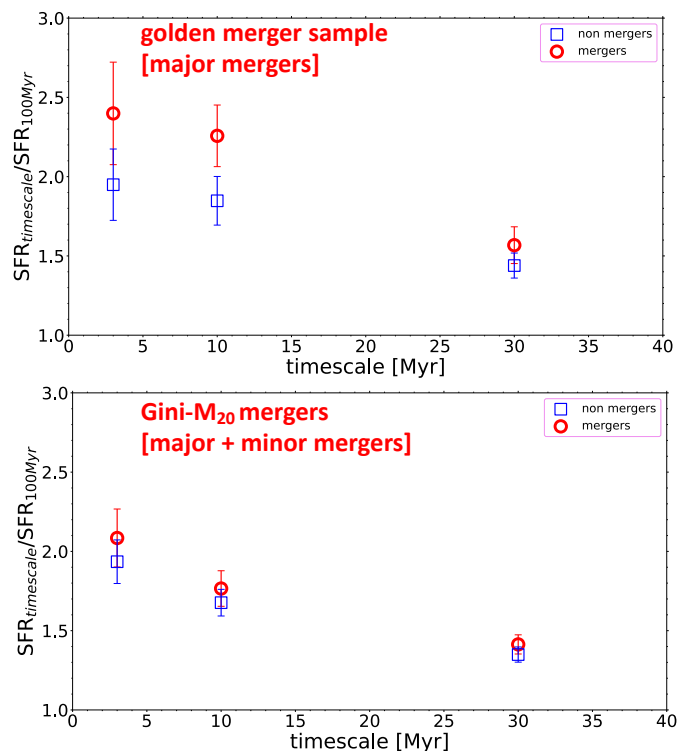


**Fig. 8.** Median burstiness parameter (y axis), defined as  $SFR_{t\text{-short}}/SFR_{100\text{Myr}}$ , of the golden merger subset (upper panel) and Gini- $M_{20}$  merger subset (bottom panel) compared to the non-merger subset (respectively, the red circles and blue squares). The comparison is shown for three different SFR timescales ‘t-short’ of 3 Myr, 10 Myr, and 30 Myr (x axis). The red and blue error bars are the uncertainties on the median burstiness of the two subsets.

matched control sample of isolated galaxies, following the same procedure described in Section 3.3.

We find burstiness parameters ranging between 0.002 and 300 for the entire sample, with median values ranging from 1.3 to 2.5 for the three timescales. In addition, more than  $\sim 75\%$  of the galaxies have a burstiness  $> 1$ , with the first and third quartiles of the distribution being  $\sim 1$  and  $\sim 4$ , respectively. This implies that the SFHs are rising on average for the stellar mass and redshift range considered in this study. The 10 Myr burstiness of the global population has a median value of  $1.9 \pm 0.2$ , and spans a similar range to those found by [Cole et al. \(2025\)](#) in a similar redshift and stellar mass range of our study, and using a similar SED fitting technique to our work.

Focusing on the golden merger sample, it has median burstiness parameter ranging from  $1.57 \pm 0.12$  for the 30 Myr timescale to  $2.4 \pm 0.3$  for the 3 Myr timescale (Fig. 8-top). The isolated galaxy sample has median burstiness values  $> 1$ , increasing toward shorter timescales, but mergers have a systematically higher burstiness than isolated galaxies for all the three timescales. The burstiness enhancement increases toward shorter SFR timescales. In the shortest timescale cases ( $< 10$  Myr) the burstiness in major mergers is a factor of  $1.22 \pm 0.12$  higher than in isolated galaxies. For the 30 Myr timescale, the difference between mergers and non mergers becomes not significant ( $1.09 \pm 0.10$ ). This suggests that the impact of major mergers on the galaxy’s SFRs mainly occurs in the last 10 Myr from the time of observation, during which they induce stronger bursts of star-formation compared to normal, isolated galaxies at the same cosmic epoch and stellar mass. The peculiar, advanced

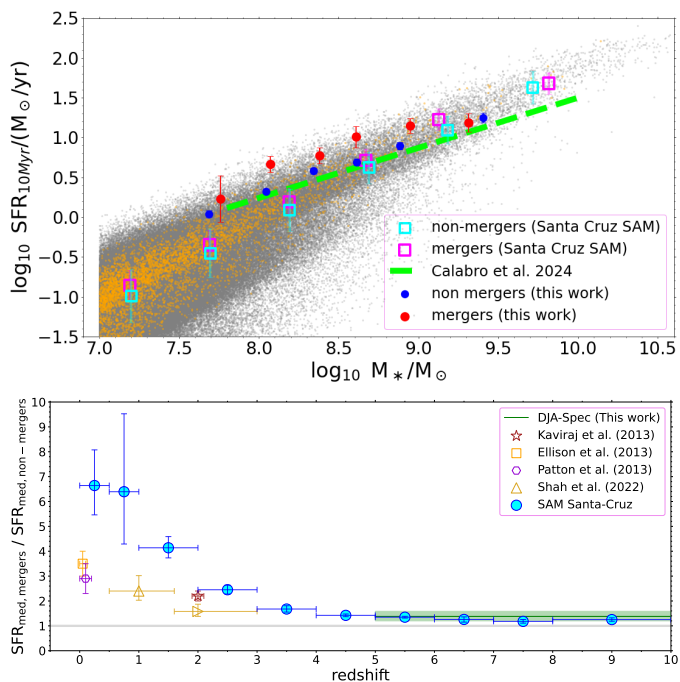


**Fig. 9.** Predictions of the Santa Cruz SAM. *Top:* SFR -  $M_{*}$  diagram for mergers (orange small circles) and non-mergers (gray small circles). The median SFRs in  $M_{*}$  bins are shown with fuchsia big empty squares and cyan empty squares, respectively for the merger and non-merger subsets. The observed SFR -  $M_{*}$  relation is shown with blue and red filled circles, respectively, for the golden merger sample and for non mergers. *Bottom:* Median SFR enhancement of the merger vs the non-merger sample ( $\text{SFR}_{\text{med,merger}}/\text{SFR}_{\text{med,non-merger}}$ ) from  $z = 0$  to  $z = 10$ , as predicted by the Santa Cruz SAM. The range of SFR enhancement observed in this work is highlighted with a green shaded rectangle.

merger phases to which we are sensitive to our morphological diagnostics provide a natural explanation to the observed results. A higher SFR enhancement in merging galaxies is observed when considering mergers with a shorter observability timescale, which are likely closer to the final coalescence. This enhanced burstiness likely reflects the bursty nature of star-formation during the merger episode.

Finally, we explore the burstiness of the Gini- $M_{20}$  sample. We find that it is generally lower than in the previous case, increasing from  $1.41 \pm 0.06$  for the 30 Myr timescale to  $2.0 \pm 0.2$  for the 3 Myr timescale (Fig. 8-bottom). However, we obtain no significant burstiness enhancements in mergers compared to the control sample for all the three SFR timescales, of  $1.08 \pm 0.12$ ,  $1.05 \pm 0.08$ , and  $1.04 \pm 0.06$ , respectively for the 3 Myr, 10 Myr, and 30 Myr timescales. This implies that major mergers likely have a higher effect on the burstiness than minor mergers, which is also consistent with the stronger enhancement of their SFRs at fixed  $M_{*}$  and redshift.

## 4. Discussion

### 4.1. Comparison to predictions of semi-analytic models and simulations

To understand our findings on the merger induced SFR enhancement across cosmic time, it is useful to compare them to the predictions of semi-analytic models of galaxy formation, and to hydro-dynamical simulations of galaxy mergers at different redshifts. First, we consider the Semi-analytic Forecasts for JWST simulation catalogue. This project makes predictions for the

distribution and properties of galaxies from  $z = 0$  to redshift 10, and is based on the Santa Cruz semi-analytic model (hereafter SC-SAM<sup>5</sup>) of galaxy formation (Somerville & Davé 2015; Somerville et al. 2021). As shown in Yung et al. (2019a) and Yung et al. (2019b), the physical framework and implementation of this model can reproduce the observed photometry of galaxies from  $z = 0$  to  $z = 10$ , and the distribution functions of fundamental galaxy properties (e.g.,  $M_{\text{UV}}$ ,  $M_{*}$ , SFR) and related scaling relations, down to the lowest masses of  $M_{*} \sim 10^7 M_{\odot}$ , which can now be reached with JWST at the EoR. More details on the physics considered in these models can be found in a series of studies (Yung et al. 2019a,b, 2020, 2022).

For this comparison, we consider the JWST ultradeep lightcones, which are a set of 8 deep-field lightcone realizations, each covering an area of  $132 \text{ arcmin}^2$ . This includes a total number of  $\sim 2$  Million simulated galaxies from  $z = 0$  to  $z = 10$ , which provides enough statistics for our work while not excessively overloading the computational effort required for the subsequent analysis. In this simulation, the lightcone contains galaxies well below those observable with JWST. For our purposes, we apply a magnitude cut of 30 in the F444W band, and a redshift selection ranging from 5 to 10 to match our observations. For each galaxy this catalog includes the information on the time since it last went through a major or minor merger, as two separate columns  $t_{\text{majormerger}}$  and  $t_{\text{merger}}$ . It also includes information on the stellar mass of the primary galaxy that went through a merger and on the instantaneous SFR, which is the quantity more directly comparable to our SFR values. In this work, we identify minor and major mergers in the models by selecting galaxies that underwent, respectively, a minor or major merger (down to mass ratios of 10:1 and 4:1) within the observability timescales defined in Section 2.7 for the Gini- $M_{20}$  and the golden merger criteria.

There are several approximations in this procedure. First, we assume that the number of galaxies that have experienced a merger in the last few Myr is the same as the number of galaxies that are going to coalesce within the same time, which are those identified by our morphological selection. In addition, the catalog associated to the simulated lightcone reports mass ratios that are based on the total baryonic mass of the galaxies (thus including gas, dust, and stars), while in the observations we consider the stellar mass ratios of colliding galaxies when defining the merger type and the corresponding observability timescale.

We now investigate the SFR - stellar mass diagram of merging and non-merging galaxies in the SC-SAM, as done for the observational data in Fig. 6. We compute the median SFR in 7 increasing stellar mass bins from  $10^7$  to  $10^{10.5} M_{\odot}$ . The results for major mergers are shown in Fig. 9-top. They indicate that the merger subset has systematically higher SFRs compared to the non-merger subset in all the stellar mass bins, with a median SFR enhancement of a factor of  $1.3 \pm 0.1$  over the whole mass and redshift range, comparable to that found in this work from observations. A similar result is obtained from the models when we also include minor mergers in the analysis.

To understand the lower SFR enhancement that we find at  $z > 5$  compared to mergers at lower redshifts, we analyze the redshift evolution of the SFR enhancement predicted by the models. To this aim, we calculate the median SFR enhancement of the merger subset in different redshift bins, from 0 to 10, adopting a uniform cut on the stellar mass as  $\log_{10} M_{*}/M_{\odot} \geq 8$ . This cut also facilitates the comparison with the other ob-

<sup>5</sup> The catalog and relevant information can be found at this webpage <https://flathub.flatironinstitute.org/sam-jwst-deep>

servational studies at similar redshifts (based on the close pair method) as mentioned in Section 3.2. In Fig. 9-bottom, we can see that the maximum SFR enhancement in mergers (by a factor of  $6_{-2}^{+3}$ ) occurs at low redshifts ( $z \leq 1$ ), while it strongly decreases by  $\sim 3.5$  times at earlier epochs between  $z = 1$  and  $z = 4$ . At  $z \geq 6$ , it stabilizes around an enhancement of 1.2.

This analysis shows that the SC-SAM predicts a strong evolution of the SFR enhancement in mergers from the local Universe to the epoch of reionization, consistent with the trend inferred from observations, despite the fact that we are comparing samples at different redshifts with slightly different selection criteria, different images available, and different merger identification methods. Most importantly, the models corroborate our results indicating that mergers have an impact on the star-formation of galaxies back to the earliest cosmic epochs that we have explored.

We also note that observations at  $z < 2$  reach a maximum enhancement of the order of  $\sim 3.5$ , significantly lower than the value predicted by the models. In Robaina et al. (2009), a SFR enhancement of 4 can be obtained if considering an Arp 220 SED template in the conversion between the luminosity at  $24\mu\text{m}$  and the total infrared luminosity for dusty starbursts. This difference might be in part due to the SFRs calculated over timescales of  $\sim 100$  Myr, while those from the models are instantaneous. Moreover, the merger duration at low redshifts significantly increases, hence the instantaneous SFRs that we use for comparison are no longer representative of the entire merger process, thus they should be interpreted as the peak SFR enhancement that can last for short periods of time.

The role of mergers in the star-formation activity of high redshift galaxies is also predicted by hydrodynamical simulations. In particular, Fensch et al. (2017) performed pc-resolution numerical simulations of mergers in the low gas fraction ( $= 10\%$ ) and high gas fraction case ( $= 60\%$ ), for different orbits (rotation and impact parameter) of the interacting galaxies. These gas fractions are typical, respectively, of  $z = 0$  and  $z = 2$  galaxies. They found that the SFR enhancement induced by the merger in the high  $f_{\text{gas}}$  case (and also the duration of this enhancement) is approximately 10 times lower than in the low  $f_{\text{gas}}$  case. More recently, Schechter et al. (2025) analyzed mergers in the Illustris TNG-50 simulation. At  $z < 0.5$ , they find that the SFR in mergers can be enhanced by a factor of  $\sim 2$  close to the final coalescence. This effect is less pronounced at higher redshifts, stabilizing around an enhancement factor of 1.5 for major mergers at  $1 < z < 3$  (the highest redshift bin of their analysis) and in the stellar mass range between  $10^8$  and  $10^9 M_{\odot}$ . This effect is comparable to that found in this study for mergers of galaxies with a similar stellar mass but at higher redshifts ( $z > 5$ ). Schechter et al. (2025) also find that a SFR enhancement at  $z = 1-3$  is also present in minor mergers, although it is slightly lower than in major mergers, in agreement with our results.

The above simulations help us to understand the physical differences between local mergers and the high redshift ones, giving an explanation of the observed results. In the local Universe, the SFR increase in mergers is caused by several factors, including enhanced gas inflows toward the galactic center (typically in the inner 1kpc), increased gas turbulence, and compressive tides induced by gravitational torques during the interaction (Renaud et al. 2008, 2009; Sparre et al. 2022). At higher redshifts the above mechanisms are already efficient in isolated systems due to the higher  $f_{\text{gas}}$  of typical star-forming galaxies, as we reach  $f_{\text{gas}} \sim 50\%$  at  $z \simeq 2$  from  $\sim 10\%$  in the local Universe (Daddi et al. 2010; Tacconi et al. 2010). Cosmological gas inflows and violent disk instabilities represent competing channels to merg-

ers for the increase of gas turbulence, inward migration of gas, and SFR increase in these galaxies (Bournaud et al. 2012; Gabor & Bournaud 2014). For example, the relative increase in baryonic mass in the central 1kpc due to merger induced inflows is approximately half the value of that in the local Universe (Fensch et al. 2017 and references therein). Another physical mechanism to consider is that at higher redshifts the fraction of galaxies with a central bulge or with a bar decreases (Sheth et al. 2008; Fragkoudi et al. 2020; Costantin et al. 2025). Therefore, the average star-forming galaxy population lacks the additional torque induced by these structures, which strongly contributes to the infall of gas in low redshift mergers.

#### 4.2. The merger rate and the contribution of mergers to the galaxy mass assembly

The merger fraction calculated above is highly dependent on the merger observability timescale of the specific tracer adopted for the merger identification. This leads to significant differences in the results when comparing studies based on different merger selection techniques. One way to remove the dependence on  $\tau_{\text{obs}}$  and assess the incidence of mergers across cosmic time is to calculate the merger rate of galaxies at different epochs. The merger rate is typically defined as :

$$\mathcal{R}_M(z, M_{\star}) = \frac{f_{\text{merge}}(z, M_{\star})}{\tau_{\text{merge}}(z)} = \frac{f_{\text{tracer}}(z, M_{\star}) \times C_{\text{merge,tracer}}}{f_{\text{obs,tracer}}(z)} \text{ (Gyr}^{-1}\text{)}, \quad (3)$$

where  $f_{\text{merge}}$  is the merger fraction, and  $\tau_{\text{merge}}$  is the dynamical time of the merger as defined in Section 2.7. Since we do not find a significant dependence of  $f_{\text{tracer}}$  on stellar mass, we simply use  $\mathcal{R}_M(z)$  in the following part of the paper, which refers to the merger rate of galaxies with a similar mass of our sample ( $M_{\star} \sim 10^7-10^9 M_{\odot}$ ). In the last part of the equation,  $f_{\text{tracer}}$  is the observed fraction of mergers for a specific merger tracer, while  $C_{\text{merge,tracer}}$  is the conversion factor between observed and real mergers. For our methodology, we can assume that  $C_{\text{merge,tracer}} = 1$ , because the morphological parameters trace secure mergers with strong asymmetric or interacting features. However, this quantity may be substantially lower, typically in the range 0.4-1, for the photometric pair method, indicating that the observed pair has a probability of 40%-100% to actually coalesce into a single galaxy at later epochs, due to uncertain redshifts, unknown relative velocities, and chance projection effects. However, the results obtained by the most recent photometric pair studies are based on the assumption that  $C_{\text{merge,tracer}} = 1$  (e.g. Duan et al. 2025; Puskás et al. 2025a). Lastly,  $\tau_{\text{obs,tracer}}(z)$  is the visibility timescale of the tracer, as introduced in Section 2.7.  $\mathcal{R}_M(z)$  allows us to compare different methods and studies on a common physical ground, because it already incorporates the intrinsically different  $\tau_{\text{obs}}$  values, even though a common  $\mu$  ratio should be also chosen, as minor and major mergers might occur at a different rate.

We derive the major merger rate taking the golden sample as our fiducial merger selection because it is more stable against variations of the gas fraction and mass ratio  $\mu$  compared to the asymmetry mergers, while for estimating the minor+major merger rate we use the Gini- $M_{20}$  selected sample. Applying in each case the corresponding observed merger fraction  $f_{\text{tracer}}$  derived in Section 3.1 and  $\tau_{\text{obs,tracer}}$  defined in Section 2.7, we obtain  $\mathcal{R}_M(z)$  as shown in the left panels of Fig. 10-11.

The major merger rate slightly increases from redshift 5 to 7.5, ranging between 1 and 3 merger events per galaxy per Gyr.

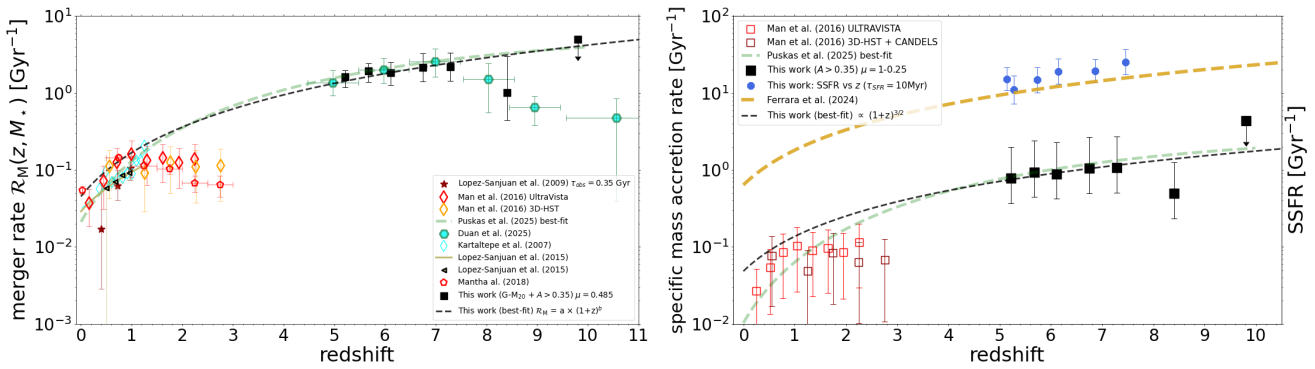


**Fig. 10.** *Left:* Merger rate derived in this study using the Gini- $M_{20}$  and  $A > 0.35$  merger criteria (black points), compared to other results from the literature at similar and lower redshifts. Our error bars incorporate the uncertainty due to the mass ratio  $\mu$  ranging between 1 and 4, typical of major mergers. The best-fit to all observed data from  $z = 0$  to  $z = 10$  is shown with a black dashed line. *Right:* sMAR due to mergers obtained in this study (black points), and in previous works at lower redshifts (red empty squares). The best-fit relation considering our observed points and low redshift results is shown with a black dashed line, while the one obtained by Puskás et al. (2025a) with the photometric pair method is drawn with a green dashed line. This quantity is compared to the redshift evolution of the sSFR from this work (blue circles) and from the model of Ferrara (2024) (golden dashed line).

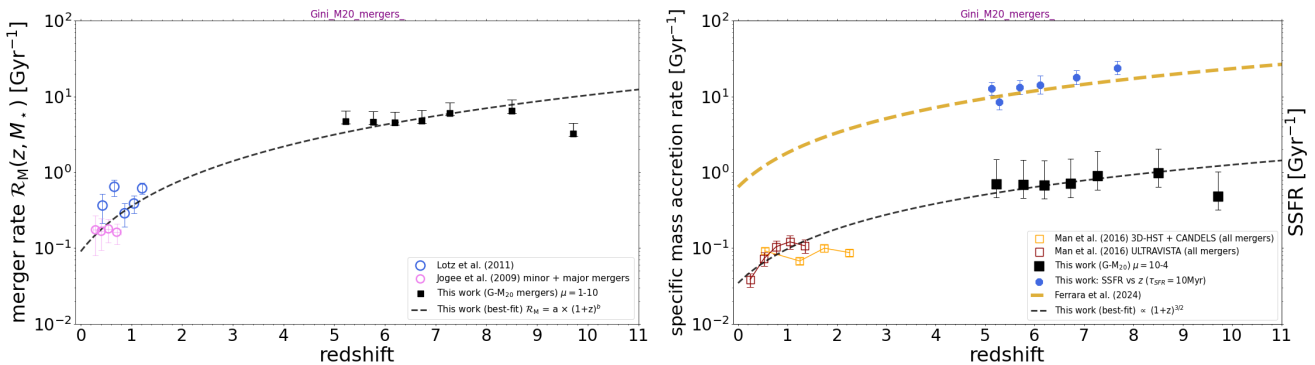


**Fig. 11.** Same as in Fig. 10, but using the Gini- $M_{20}$  criterion only, which likely probes major and minor mergers down to a mass ratio  $\mu = 10$ .

At later epochs ( $z > 7.5$ ),  $\mathcal{R}_M(z)$  drops again to 1 merger per galaxy per Gyr. However, given the larger uncertainty, it would still be consistent with the average increasing trend obtained from the lower redshift bins. Remarkably, once we take the different observability timescales into account, our morphological method provides major merger rates that are consistent to those obtained from the photometric pair method by Duan et al. (2025) and Puskás et al. (2025a) in the same redshift range and at similar stellar masses. If we compare this result to lower redshift studies, we can immediately notice that, in contrast with the almost flat trend of the merger fraction, the merger rate shows a strong evolution from  $z = 0$  to  $z = 10$  by more than one order of magnitude, going from  $\leq 0.1$  merger/galaxy/Gyr at  $z \leq 1$  to  $\geq 1$  merger/galaxy/Gyr at  $z > 5$ . Considering both the high redshift and low redshift ( $z < 1$ ) data points (López-Sanjuan et al. 2009, 2015; Mantha et al. 2018; Kartaltepe et al. 2007; Man et al. 2016), we can fit the major merger rate evolution with a similar function to that adopted in Conselice et al. (2022) as:

$$\mathcal{R}_M(z) = a \times (1+z)^b, \quad (4)$$

with  $a = 0.045 \pm 0.009$  and  $b = 1.9 \pm 0.1$ . For the minor+major merger rate traced by the Gini- $M_{20}$  parameters, it follows a similar redshift trend as the major merger rate but with systematically higher values, going from  $\sim 4$  mergers/galaxy/Gyr at  $z \simeq 5$  to  $\sim 7$  mergers/galaxy/Gyr at  $z \simeq 7$ , before dropping at  $\sim 3$  mergers/galaxy/Gyr in the last redshift bin ( $z > 9$ ). The average  $\mathcal{R}_M$  across the entire range  $5 < z < 10$  is  $5.0 \pm 0.3$  mergers/galaxy/Gyr. The merger rate values estimated in different redshift bins are reported in the appendix B in Table B.3.

Using Equation 4 to fit our data in combination with low redshift ( $z < 1.5$ ) studies (Lotz et al. 2011; Jogee et al. 2009), we obtain  $a = 0.09 \pm 0.01$  and  $b = 2.0 \pm 0.1$ . This again indicates a strong evolution of the ‘total’ merger rate across  $\sim 12$  Gyr of cosmic history, with mergers becoming more numerous and more frequent in the early Universe. We note that, even though the merger rate at  $z > 5$  is much higher, the amount of mass added per merger is presumably lower than in the local universe, due to the typical smaller masses of high redshift galaxies compared to the samples analyzed at lower  $z$ .

We can finally estimate the contribution of mergers to the stellar mass growth of galaxies across different epochs. In particular, we calculate the specific mass accretion rate (sMAR) of mergers using the formalism of Duncan et al. (2019) and Puskás et al. (2025a), as :

$$sMAR(z) = \mathcal{R}_M(z) \times \bar{\mu}, \quad (5)$$

where  $\mathcal{R}_M(z)$  is defined in Equation 4 and  $\bar{\mu}$  is the average mass ratio of the sample. For the major merger case, we considered the value  $\bar{\mu} = 0.485$  calculated by Puskás et al. (2025a) in their photometric sample. However, the associated error bars are derived by assuming that  $\bar{\mu}$  can vary in a range from 0.25 to 1. For the total (minor+major) merger sMAR, we instead considered a  $\bar{\mu} = 0.15$  (Lotz et al. 2011), with error bars incorporating a  $\bar{\mu}$  variation between 0.1 and 1.

With these assumptions, we find that, in the entire redshift range of our analysis ( $5 < z < 10$ ), the sMAR varies between 0.5 and 1  $\text{Gyr}^{-1}$  with median of  $0.92 \pm 0.08$  and  $0.71 \pm 0.06$ ,

respectively for the major and major+minor merger sample (see right panels of Fig. 10-11). As for the  $\mathcal{R}_M(z)$ , the lower sMAR found for major mergers in the highest redshift bin has a higher uncertainty and is still consistent with the global increasing trend derived at lower redshifts. We report the sMAR in different redshift bins in Table B.3.

The merger induced sMAR at redshifts  $5 < z < 10$  is approximately an order of magnitude smaller than the specific mass accretion due to star-formation, which is by definition the sSFR. We use for our sample the SFRs averaged over a timescale of 10 Myr, which yields sSFR( $z$ ) in reasonable agreement with the theoretical evolution derived in Ferrara (2024) as  $0.64 \times (1+z)^{1.5}$ . As shown in Fig. 10-11, the merger contribution to the galaxy mass assembly varies between 5% and 10%, much lower than the contribution from (in-situ) star-formation in non-merging galaxies.

If we also fit the sMAR derived at  $z < 3$  by Man et al. (2016), we find that the sMAR( $z$ ) mimicks the evolution of the sSFR( $z$ ), and can be well fit by a power-law function with the same exponent as  $c \times (1+z)^{1.5}$ , with the constant  $c = 0.048 \pm 0.002$  for the major merger sample and  $c = 0.052 \pm 0.003$  for the total merger sample. Therefore, mergers provide a lower contribution to the build up of galaxies compared to secular star-formation at all cosmic epochs, and do not play a bigger role in the early Universe. This is consistent with the conclusions of Puskás et al. (2025a), whose sMAR( $z$ ) for major mergers is in remarkable agreement with our results (Fig. 10-right). We finally note that assuming a longer observability timescale (up to 100 Myr) for our morphological merger criteria, the merger rates and the sMAR would be  $\sim 0.47$  dex lower, strenghtening our conclusions on the minor role of mergers in galaxy mass assembly.

## 5. Summary and conclusions

We have investigated the merger fraction at  $z > 5$  in a spectroscopically selected sample of galaxies, with mergers identified based on rest-frame optical morphological disturbances (traced by the Gini,  $M_{20}$ , and asymmetry parameters) in F444W NIR-Cam images. This provides a complementary approach, tracing shorter merger phases, to the close photometric pairs adopted in similar previous studies. We have also explored the role of mergers in the star-formation rate enhancement in the early Universe, and their contribution to the galaxy mass build-up across different epochs. We summarize our findings as follows :

- the morphological merger fraction does not strongly evolve with redshift, remaining approximately constant from  $z \simeq 1$  to the redshifts explored in this study ( $5 < z < 8$ ), and eventually decreasing at  $z > 8$ .
- the absolute value of the merger fraction depends on the type of merger and on the merger observability timescale traced by each morphological parameter, increasing for minor mergers and for longer merger observabilities. In particular, it varies from  $\sim 5\%$  for the gold merger sample (which traces major mergers with  $\tau_{obs} \simeq 200$  Myr at  $z \sim 1$ ), to  $\sim 8\%$  for Asymmetry mergers having longer observability timescales of  $\simeq 400$  Myr at  $z = 1$ . The merger fractions further increase to  $\sim 13\%$  for the Gini- $M_{20}$  mergers, which likely trace minor+major mergers (down to a mass ratio  $\mu = 10$ ) with  $\tau_{obs,z=1} \simeq 200$  Myr.
- mergers at redshifts  $5 < z < 10$  have a significant impact (although much lower than at  $z < 1$ ) on the star-formation rate of galaxies, with an average enhancement by a factor of  $\sim 1.7$  compared to a mass and redshift matched sample of undisturbed star-forming galaxies. The SFR enhancement

is higher for shorter timescale SFRs ( $< 10$  Myr) and for morphological indicators with shorter merger observability timescales, in agreement with a short-lived, bursty nature of merger triggered star-formation.

- after accounting for the observability timescale of each merger tracer and for the redshift evolving merger dynamical time, we find major merger rates of  $\sim 2$  merger/galaxy/Gyr on average at redshifts  $5 < z < 10$ , and a factor of  $\sim 3$  higher for minor+major mergers. Combined with low redshift results, the merger rates show a strong evolution in redshift, increasing approximately by one order of magnitude from  $z = 1$  to  $z = 7$ , as due to the intrinsically shorter merger duration in the early Universe. The major merger rate is also in agreement with that inferred using the close pair method with photometric galaxy samples in a similar mass and redshift range of this study. Despite the higher merger rate, the amount of mass added per merger at  $z > 5$  is likely lower than at  $z < 1$ , due to the typical smaller masses of high- $z$  galaxies compared to those probed at lower  $z$ .
- we find that mergers with a mass ratio  $\mu > 10$  contribute  $\sim 5-10\%$  to the mass build-up of galaxies at  $5 < z < 10$  compared to in-situ star-formation, suggesting that mergers are not the dominant process in galaxy growth as in the low redshift Universe.

This study sets the groundbase for a more detailed investigation of the effects of mergers on other galaxy properties, including dust attenuation, metallicity, ionization, and ionizing continuum escape, through the use of spectroscopic data. In the future, this work will benefit from the growing number of spatially resolved spectroscopic observations, which will allow us to explore where most of the star-formation occurs during merger events. Moreover, future imaging observations with the Extremely Large Telescope (ELT), thanks to its greater sensitivity and resolution compared to JWST, will enable an increase in the statistics of mergers in the early Universe and in low-mass regime ( $M_* < 10^7 M_\odot$ ), and the identification of late-stage mergers with very close nuclei or post-merger systems with faint residual interaction features.

*Acknowledgements.* The research activities described in this paper were carried out with contribution of the Next Generation EU funds within the National Recovery and Resilience Plan (PNRR), Mission 4 – Education and Research, Component 2 – From Research to Business (M4C2), Investment Line 3.1 – Strengthening and creation of Research Infrastructures, Project IR0000034–“STILES – Strengthening the Italian Leadership in ELT and SKA”. We acknowledge support from the PRIN 2022 MUR project 2022CB3PJ3 - First Light And Galaxy aSsembly (FLAGS) funded by the European Union – Next Generation EU.

## References

- Astropy Collaboration, Price-Whelan, A. M., Lim, P. L., et al. 2022, ApJ, 935, 2, 167.
- Barnes, J. E. 1992, ApJ, 393, 484.
- Bezanson, R., Labbe, I., Whitaker, K. E., et al. 2024, ApJ, 974, 1, 92.
- Bottrell, C., Hani, M. H., Teimoorinia, H., et al. 2019, MNRAS, 490, 4, 5390.
- Bournaud, F., Juneau, S., Le Floch, E., et al. 2012, ApJ, 757, 1, 81.
- Bradley, L. 2023, Zenodo, 1.8.0.
- Brammer, G. 2023, Zenodo, 0.6.17.
- Brammer, G. 2023, Zenodo, 1.9.11.
- Bunker, A. J., Cameron, A. J., Curtis-Lake, E., et al. 2024, A&A, 690, A288.
- Calabrò, A., Pentericci, L., Santini, P., et al. 2024, A&A, 690, A290.
- Calabrò, A., Daddi, E., Fensch, J., et al. 2019, A&A, 632, A98.
- Calzetti, D., Armus, L., Bohlin, R. C., et al. 2000, ApJ, 533, 2, 682.
- Carnall, A. C., McLure, R. J., Dunlop, J. S., et al. 2018, MNRAS, 480, 4, 4379.
- Chabrier, G. 2003, PASP, 115, 809, 763.
- Cibinel, A., Daddi, E., Sargent, M. T., et al. 2019, MNRAS, 485, 4, 5631.
- Coe, D., Bradley, L., & Zitrin, A. 2015, ApJ, 800, 2, 84.
- Cole, J. W., Papovich, C., Finkelstein, S. L., et al. 2025, ApJ, 979, 2, 193.

- Conselice, C. J., Bershady, M. A., Dickinson, M., et al. 2003, *Aj*, 126, 3, 1183.
- Conselice, C. J., Bershady, M. A., & Jangren, A. 2000, *ApJ*, 529, 2, 886.
- Conselice, C. J. 2007, *Galaxy Evolution across the Hubble Time*, 235, 381.
- Conselice, C. J., Yang, C., & Bluck, A. F. L. 2009, *MNRAS*, 394, 4, 1956.
- Conselice, C. J. & Arnold, J. 2009, *MNRAS*, 397, 1, 208.
- Conselice, C. J., Mundy, C. J., Ferreira, L., et al. 2022, *ApJ*, 940, 2, 168.
- Costantin, L., Gillman, S., Boogaard, L. A., et al. 2025, *A&A*, 699, A360.
- Daddi, E., Bournaud, F., Walter, F., et al. 2010, *ApJ*, 713, 1, 686.
- Dalmaso, N., Calabrò, A., Leethochawalit, N., et al. 2024, *MNRAS*, 533, 4, 4472.
- de Graaff, A., Rix, H.-W., Carniani, S., et al. 2024, *A&A*, 684, A87.
- de Graaff, A., Brammer, G., Weibel, A., et al. 2025, *A&A*, 697, A189.
- Di Matteo, P., Bournaud, F., Martig, M., et al. 2008, *A&A*, 492, 1, 31.
- Dottorini, D., Calabrò, A., Pentericci, L., et al. 2025, *A&A*, 698, A234.
- Duan, Q., Conselice, C. J., Li, Q., et al. 2025, *MNRAS*, 540, 1, 774.
- Duan, Q., Conselice, C. J., Harvey, T., et al. 2026, *MNRAS*, 546, 3, stag008.
- Duncan, K., Conselice, C. J., Mundy, C., et al. 2019, *ApJ*, 876, 2, 110.
- Eisenstein, D. J., Johnson, B. D., Robertson, B., et al. 2025, *ApJs*, 281, 2, 50.
- Endsley, R., Stark, D. P., Whitler, L., et al. 2024, *MNRAS*, 533, 1, 1111.
- Fensch, J., Renaud, F., Bournaud, F., et al. 2017, *MNRAS*, 465, 2, 1934.
- Ferland, G. J., Chatzikos, M., Guzmán, F., et al. 2017, *RevMexAA*, 53, 385.
- Ferrara, A. 2024, *A&A*, 684, A207.
- Ferreira, L., Conselice, C. J., Duncan, K., et al. 2020, *ApJ*, 895, 2, 115.
- Finkelstein, S. L., Bagley, M. B., Ferguson, H. C., et al. 2023, *ApJL*, 946, 1, L13.
- Finkelstein, S. L., Bagley, M. B., Arrabal Haro, P., et al. 2025, *ApJL*, 983, 1, L4.
- Fragkoudi, F., Grand, R. J. J., Pakmor, R., et al. 2020, *MNRAS*, 494, 4, 5936.
- Gabor, J. M. & Bournaud, F. 2014, *MNRAS*, 437, 1, L56.
- Gehrels, N. 1986, *ApJ*, 303, 336.
- Grogin, N. A., Kocevski, D. D., Faber, S. M., et al. 2011, *ApJs*, 197, 2, 35.
- Gutkin, J., Charlot, S., & Bruzual, G. 2016, *MNRAS*, 462, 2, 1757.
- Guzmán-Ortega, A., Rodríguez-Gomez, V., Snyder, G. F., et al. 2023, *MNRAS*, 519, 4, 4920.
- Heintz, K. E., Brammer, G. B., Giménez-Arteaga, C., et al. 2023, *Nature Astronomy*, 7, 1517.
- Heintz, K. E., Brammer, G. B., Watson, D., et al. 2025, *A&A*, 693, A60.
- Holwerda, B. W., Pirzkal, N., de Blok, W. J. G., et al. 2011, *MNRAS*, 416, 4, 2415.
- Hopkins, P. F., Hernquist, L., Cox, T. J., et al. 2008, *ApJs*, 175, 2, 356.
- Huertas-Company, M., Gravet, R., Cabrera-Vives, G., et al. 2015, *ApJs*, 221, 1, 8.
- Huertas-Company, M., Primack, J. R., Dekel, A., et al. 2018, *ApJ*, 858, 2, 114.
- Inoue, A. K., Shimizu, I., Iwata, I., et al. 2014, *MNRAS*, 442, 2, 1805.
- Jogee, S., Miller, S. H., Penner, K., et al. 2009, *ApJ*, 697, 2, 1971.
- Kartaltepe, J. S., Sanders, D. B., Scoville, N. Z., et al. 2007, *ApJs*, 172, 1, 320.
- Kartaltepe, J. S., Mozena, M., Kocevski, D., et al. 2015, *ApJs*, 221, 1, 11.
- Kartaltepe, J. S., Rose, C., Vanderhoof, B. N., et al. 2023, *ApJL*, 946, 1, L15.
- Koekemoer, A. M., Faber, S. M., Ferguson, H. C., et al. 2011, *ApJs*, 197, 2, 36.
- Kormendy, J. & Kennicutt, R. C. 2004, *ARA&A*, 42, 1, 603.
- Lehnert, M. D., van Driel, W., & Minchin, R. 2016, *A&A*, 590, A51.
- Leja, J., Carnall, A. C., Johnson, B. D., et al. 2019, *ApJ*, 876, 1, 3.
- Liang, L., Feldmann, R., Murray, N., et al. 2024, *MNRAS*, 528, 1, 499.
- Lisker, T. 2008, *ApJs*, 179, 2, 319.
- Llerena, M., Amorín, R., Pentericci, L., et al. 2024, *A&A*, 691, A59.
- Llerena, M., Pentericci, L., Amorín, R., et al. 2025, arXiv:2510.25647.
- López-Sanjuan, C., Balcells, M., Pérez-González, P. G., et al. 2009, *A&A*, 501, 2, 505.
- López-Sanjuan, C., Cenarro, A. J., Varela, J., et al. 2015, *A&A*, 576, A53.
- Lotz, J. M., Primack, J., & Madau, P. 2004, *Aj*, 128, 1, 163.
- Lotz, J. M., Jonsson, P., Cox, T. J., et al. 2008, *MNRAS*, 391, 3, 1137.
- Lotz, J. M., Davis, M., Faber, S. M., et al. 2008, *ApJ*, 672, 1, 177.
- Lotz, J. M., Jonsson, P., Cox, T. J., et al. 2010, *MNRAS*, 404, 2, 590.
- Lotz, J. M., Jonsson, P., Cox, T. J., et al. 2011, *ApJ*, 742, 2, 103.
- Lotz, J., Mountain, M., Grogin, N. A., et al. 2014, *A&A*, 223, 254.01.
- Man, A. W. S., Zirm, A. W., & Toft, S. 2016, *ApJ*, 830, 2, 89.
- Mantha, K. B., McIntosh, D. H., Brennan, R., et al. 2018, *MNRAS*, 475, 2, 1549.
- Margalef-Bentabol, B., Wang, L., La Marca, A., et al. 2024, *A&A*, 687, A24.
- Mascia, S., Roberts-Borsani, G., Treu, T., et al. 2024, *A&A*, 690, A2.
- Merlin, E., Pilo, S., Fontana, A., et al. 2019, *A&A*, 622, A169.
- Merlin, E., Santini, P., Paris, D., et al. 2024, *A&A*, 691, A240.
- Mundy, C. J., Conselice, C. J., Duncan, K. J., et al. 2017, *MNRAS*, 470, 3, 3507.
- Naab, T., Oser, L., Emsellem, E., et al. 2014, *MNRAS*, 444, 4, 3357.
- Oke, J. B. & Gunn, J. E. 1983, *ApJ*, 266, 713.
- Patton, D. R., Torrey, P., Ellison, S. L., et al. 2013, *MNRAS*, 433, 1, L59.
- Pawlik, M. M., Wild, V., Walcher, C. J., et al. 2016, *MNRAS*, 456, 3, 3032.
- Pearson, W. J., Wang, L., Trayford, J. W., et al. 2019, *A&A*, 626, A49.
- Pearson, W. J., Wang, L., Alpaslan, M., et al. 2019, *A&A*, 631, A51.
- Petty, S. M., Armus, L., Charmandaris, V., et al. 2014, *Aj*, 148, 6, 111.
- Polletta, M., Frye, B. L., Garuda, N., et al. 2024, *A&A*, 690, A285.
- Puskás, D., Tacchella, S., Simmonds, C., et al. 2025, *MNRAS*, 540, 3, 2146.
- Puskás, D., Tacchella, S., Simmonds, C., et al. 2025, arXiv:2510.14743.
- Renaud, F., Boily, C. M., Fleck, J.-J., et al. 2008, *MNRAS*, 391, 1, L98.
- Renaud, F., Boily, C. M., Naab, T., et al. 2009, *ApJ*, 706, 1, 67.
- Robaina, A. R., Bell, E. F., Skelton, R. E., et al. 2009, *ApJ*, 704, 1, 324.
- Rodríguez-Gomez, V., Snyder, G. F., Lotz, J. M., et al. 2019, *MNRAS*, 483, 3, 4140.
- Rodríguez-Gomez, V. 2019, Zenodo, v0.3.3.
- Rose, C., Kartaltepe, J. S., Snyder, G. F., et al. 2023, *ApJ*, 942, 1, 54.
- Salvador, D., Cerulo, P., Valenzuela, K., et al. 2024, *A&A*, 684, A166.
- Sazonova, E., Morgan, C., Balogh, M., et al. 2024, *The Open Journal of Astrophysics*, 7, 77.
- Sazonova, E., Morgan, C. R., Balogh, M., et al. 2025, arXiv:2511.09644.
- Schechter, A. L., Genel, S., Terrazas, B., et al. 2025, *ApJ*, 989, 2, 149.
- Shah, E. A., Kartaltepe, J. S., Magagnoli, C. T., et al. 2022, *ApJ*, 940, 1, 4.
- Sheth, K., Elmegreen, D. M., Elmegreen, B. G., et al. 2008, *ApJ*, 675, 2, 1141.
- Snyder, G. F., Lotz, J., Moody, C., et al. 2015, *MNRAS*, 451, 4, 4290.
- Snyder, G. F., Lotz, J. M., Rodríguez-Gomez, V., et al. 2017, *MNRAS*, 468, 1, 207.
- Snyder, G. F., Rodríguez-Gomez, V., Lotz, J. M., et al. 2019, *MNRAS*, 486, 3, 3702.
- Somerville, R. S. & Davé, R. 2015, *ARA&A*, 53, 51.
- Somerville, R. S., Olsen, C., Yung, L. Y. A., et al. 2021, *MNRAS*, 502, 4, 4858.
- Sparre, M., Whittingham, J., Damle, M., et al. 2022, *MNRAS*, 509, 2, 2720.
- Tacconi, L. J., Genzel, R., Neri, R., et al. 2010, *Nature*, 463, 7282, 781.
- Thorp, M. D., Bluck, A. F. L., Ellison, S. L., et al. 2021, *MNRAS*, 507, 1, 886.
- Toomre, A. & Toomre, J. 1972, *ApJ*, 178, 623.
- Treu, T., Roberts-Borsani, G., Bradac, M., et al. 2022, *ApJ*, 935, 2, 110.
- Treu, T., Calabrò, A., Castellano, M., et al. 2023, *ApJL*, 942, 2, L28.
- Valentino, F., Heintz, K. E., Brammer, G., et al. 2025, *A&A*, 699, A358.
- Vulcani, B., Treu, T., Calabrò, A., et al. 2023, *ApJL*, 948, 2, L15.
- Westcott, L., Conselice, C. J., Harvey, T., et al. 2025, *ApJ*, 983, 2, 121.
- Whitney, A., Conselice, C. J., Duncan, K., et al. 2020, *ApJ*, 903, 1, 14.
- Whitney, A., Ferreira, L., Conselice, C. J., et al. 2021, *ApJ*, 919, 2, 139.
- Yao, Y., Song, J., Kong, X., et al. 2023, *ApJ*, 954, 2, 113.
- Yung, L. Y. A., Somerville, R. S., Popping, G., et al. 2019, *MNRAS*, 490, 2, 2855.
- Yung, L. Y. A., Somerville, R. S., Finkelstein, S. L., et al. 2019, *MNRAS*, 483, 3, 2983.
- Yung, L. Y. A., Somerville, R. S., Finkelstein, S. L., et al. 2020, *MNRAS*, 496, 4, 4574.
- Yung, L. Y. A., Somerville, R. S., Ferguson, H. C., et al. 2022, *MNRAS*, 515, 4, 5416.

## Appendix A: Definition of morphological parameters

We briefly present here the main definition of the three morphological parameters adopted in this study (Gini,  $M_{20}$ , and asymmetry), while referring to previous papers for further details. The Gini coefficient is defined as :

$$G = \frac{1}{\bar{X}n(n-1)} \sum_i^n (2i - n - 1)X_i \quad (\text{A.1})$$

where  $X_i$  is the intensity of the  $i^{\text{th}}$  pixel,  $n$  is the total number of pixels of the galaxy, and  $\bar{X}$  is the mean intensity. The Gini parameter varies between 0 and 1 by construction, distinguishing between galaxies with more homogeneous flux distributions (low Gini) and more unequal flux distributions (high Gini), which is more typical of mergers. In all cases, the pixels are assigned to the galaxy based on the segmentation map derived through the *photutils* package following [Treu et al. \(2023\)](#), and adopting a flux threshold for detection of  $3\sigma$  above the background.

The second-order moment of brightness  $M_{20}$ , is defined as :

$$M_{20} = \log_{10} \left( \frac{\sum_i M_i}{M_{\text{tot}}} \right), \text{ with } \sum_i f_i < 0.2f_{\text{tot}} \quad (\text{A.2})$$

([Lotz et al. 2004](#)), where  $f_{\text{tot}}$  is the total flux of the galaxy pixels,  $M_i$  is the second-order moment of brightness of each pixel, and  $M_{\text{tot}} = \sum_i^n M_i = \sum_i^n f_i [(x_i - x_c)^2 + (y_i - y_c)^2]$ , where  $f_i$  is the pixel intensity,  $x_i$  and  $y_i$  are the pixel coordinates, and  $x_c$  and  $y_c$  represent the galaxy center where  $M_{\text{tot}}$  is minimized. The sum is done over the brightest 20% pixels of the galaxy identified through the segmentation map.  $M_{20}$  typically varies between  $-3$  and  $0$ . Smooth, normal galaxies have lower  $M_{20}$ , while the presence of bright off-centered structures, such as multiple nuclei and tidal tails, tend to increase  $M_{20}$ . As a result, merger systems typically have higher values of this parameter.

Lastly, the asymmetry ( $A$ ) is defined as:

$$A = \frac{\sum |I - I_\pi|}{\sum I} - A_{\text{bkg}} \quad (\text{A.3})$$

([Conselice et al. 2000](#)) where  $I$  is the original cutout image,  $I_\pi$  is the image rotated by 180 degrees, and  $A_{\text{bkg}}$  is the asymmetry of the background. Also this quantity varies between 0 and 1, with merging galaxies having higher values as due to their asymmetric and more irregular structure compared to non-mergers.

## Appendix B: Tables

### Appendix C: Cutouts of galaxies

**Table B.1.** Merger fraction and median galaxy properties in the redshift bins analysed in this work

$z_{\text{med}}$	$\log_{10} M_{*,\text{med}}/M_\odot$	$N_{\text{galaxies}}$	$f_m^1$	$f_m^2$	$f_m^3$
5.22	8.72	438	$0.05^{0.02}_{0.01}$	$0.08^{0.02}_{0.01}$	$0.17^{0.02}_{0.02}$
5.68	8.50	343	$0.05^{0.02}_{0.01}$	$0.07^{0.02}_{0.02}$	$0.14^{0.02}_{0.02}$
6.11	8.51	103	$0.05^{0.03}_{0.02}$	$0.07^{0.03}_{0.02}$	$0.13^{0.05}_{0.03}$
6.75	8.68	111	$0.05^{0.04}_{0.02}$	$0.07^{0.04}_{0.02}$	$0.12^{0.05}_{0.03}$
7.29	8.50	169	$0.04^{0.04}_{0.02}$	$0.05^{0.04}_{0.02}$	$0.13^{0.04}_{0.03}$
8.68	8.4	43	$0.02^{0.05}_{0.01}$	$0.02^{0.05}_{0.01}$	$0.12^{0.08}_{0.05}$
9.85	8.56	21	$< 0.07$	$< 0.07$	$0.05^{0.13}_{0.04}$

**Notes.** The first three columns indicate, respectively, the median redshift, the median stellar mass, and the total number of galaxies for each redshift bin, as defined in the text. The last three columns include the merger fraction (with  $1\sigma$  uncertainties).  $f_m^1$ : **gold merger sample (Gini- $M_{20} + A > 0.35$ )**;  $f_m^2$ : **Asymmetry mergers ( $A > 0.35$ )**;  $f_m^3$ : **Gini- $M_{20}$  mergers (Gini +  $0.14 \times M_{20} \geq 0.33$ )**

**Table B.2.** SFR and sSFR enhancement in mergers at  $z > 5$

SFR - stellar mass relation			
$\log_{10} M_{*,\text{med}}/M_\odot$	$\log_{10} \text{SFR}_{\text{med}}^{\text{NM}}$	$\log_{10} \text{SFR}_{\text{med}}^{M,1}$	$\log_{10} \text{SFR}_{\text{med}}^{M,2}$
	$M_\odot/\text{yr}$	$M_\odot/\text{yr}$	$M_\odot/\text{yr}$
7.7	$0.04 \pm 0.04$	$0.29 \pm 0.16$	$0.2 \pm 0.3$
8.1	$0.32 \pm 0.04$	$0.49 \pm 0.09$	$0.66 \pm 0.1$
8.4	$0.58 \pm 0.04$	$0.87 \pm 0.06$	$0.77 \pm 0.1$
8.6	$0.69 \pm 0.04$	$1.01 \pm 0.19$	$1.01 \pm 0.13$
8.9	$0.9 \pm 0.05$	$1.04 \pm 0.17$	$1.15 \pm 0.09$
9.4	$1.25 \pm 0.06$	$1.23 \pm 0.23$	$1.19 \pm 0.12$

Redshift evolution of the sSFR				
$z_{\text{med}}$	$\log_{10} \text{sSFR}_{\text{med}}^{\text{NM},1}$	$\log_{10} \text{sSFR}_{\text{med}}^{M,1}$	$\log_{10} \text{sSFR}_{\text{med}}^{\text{NM},2}$	$\log_{10} \text{sSFR}_{\text{med}}^{M,2}$
	1/Gyr	1/Gyr	1/Gyr	1/Gyr
5.1	$1.11 \pm 0.15$	$1.4 \pm 0.18$	$1.06 \pm 0.08$	$1.28 \pm 0.11$
5.3	$0.91 \pm 0.15$	$1.13 \pm 0.17$	$0.87 \pm 0.07$	$1.1 \pm 0.11$
5.6	$1.06 \pm 0.16$	$1.4 \pm 0.2$	$1.05 \pm 0.08$	$1.24 \pm 0.15$
6.0	$1.19 \pm 0.15$	$1.4 \pm 0.16$	$1.03 \pm 0.1$	$1.05 \pm 0.12$
6.8	$1.26 \pm 0.1$	$1.45 \pm 0.22$	$1.22 \pm 0.08$	$1.37 \pm 0.13$
7.6	$1.39 \pm 0.13$	$1.42 \pm 0.19$	$1.35 \pm 0.07$	$1.43 \pm 0.11$

**Notes.** The upper table includes the median SFR in  $M_*$  bins for the golden merger sample (label  $M,1$ ), Gini- $M_{20}$  mergers (label  $M,2$ ), and non-merger sample (label  $\text{NM}$ ), as shown in Fig.6. The lower table includes the median sSFR in  $z$  bins for the merger and non-merger samples, as shown in Fig.7. The labels  $\text{NM},1$  and  $\text{NM},2$  refer to the control sample of non-merger galaxies of the golden merger sample and Gini- $M_{20}$  mergers, respectively.

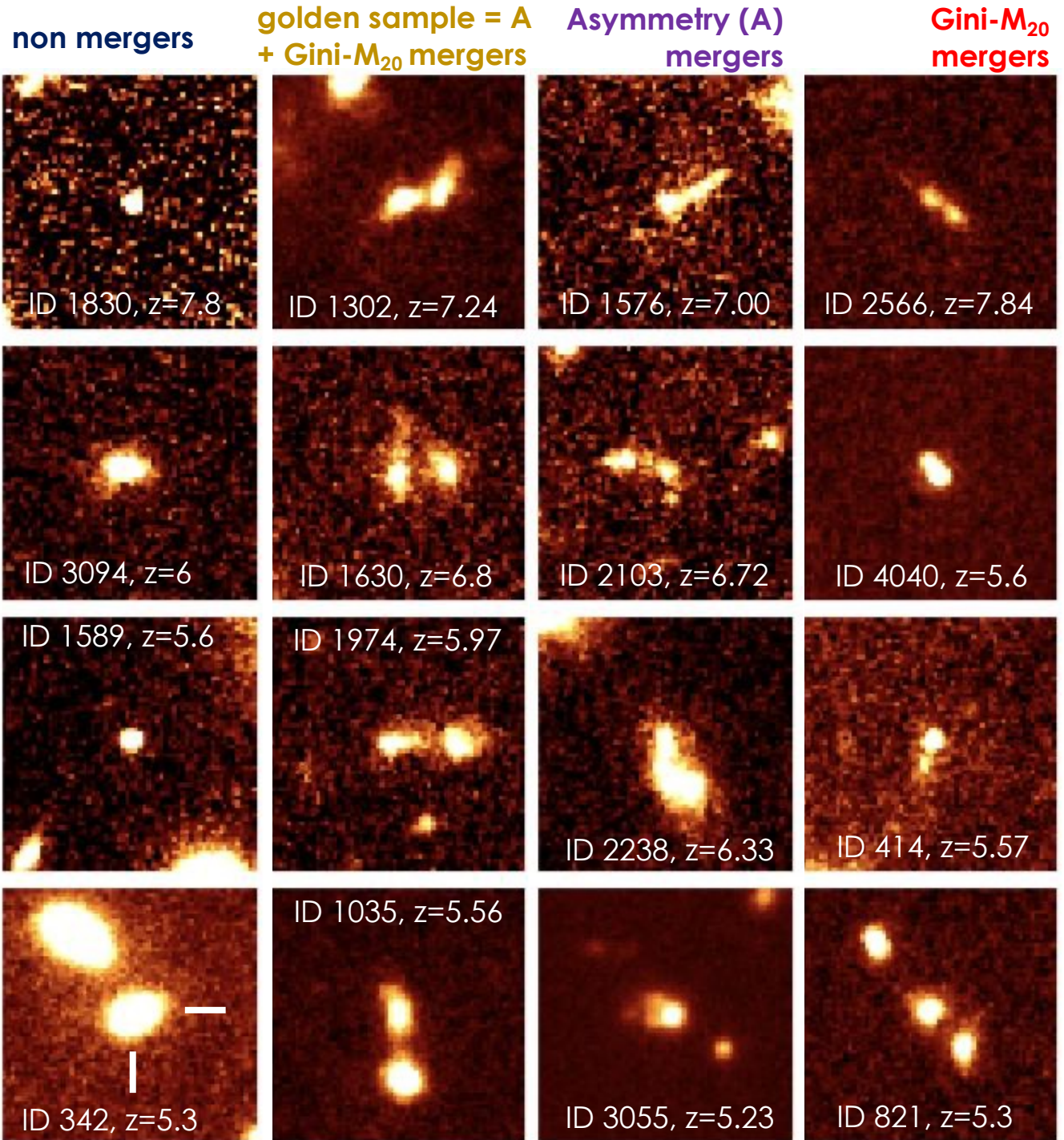


**Fig. C.1.**  $3'' \times 3''$  F444W cutouts of example galaxies selected in this work and belonging to different morphological classes, as defined in Section 2.6. The columns include, from left to right, non-merger galaxies, gold mergers, asymmetry mergers, and Gini- $M_{20}$  mergers, representing each quadrant of Fig. 3 (respectively, the bottom-left, top-right, bottom-right, and top-left corners). For each column, galaxies are shown in decreasing order of redshift (from top to bottom).

**Table B.3.** Merger rates and specific mass accretion rates due to mergers for the sample analyzed in this work

$z_{\text{med}}$	$\mathcal{R}_M^1$	sMAR <sup>1</sup>	$\mathcal{R}_M^2$	sMAR <sup>2</sup>
5.22	$1.6_{0.4}^{0.1}$	$0.8_{0.4}^{1.2}$	$4.70_{0.15}^{1.8}$	$0.7_{0.2}^{0.8}$
5.77	$1.9_{0.5}^{0.2}$	$0.9_{0.5}^{1.4}$	$4.62_{0.15}^{1.8}$	$0.7_{0.2}^{0.8}$
6.20	$1.8_{0.4}^{0.2}$	$0.9_{0.5}^{1.4}$	$4.54_{0.15}^{1.8}$	$0.7_{0.2}^{0.8}$
6.73	$2.2_{0.5}^{0.2}$	$1.1_{0.6}^{1.6}$	$4.76_{0.16}^{1.9}$	$0.7_{0.2}^{0.8}$
7.28	$2.2_{0.5}^{0.2}$	$1.1_{0.6}^{1.6}$	$6.00_{0.19}^{2.3}$	$0.9_{0.3}^1$
8.50	$1.0_{0.2}^{0.08}$	$0.5_{0.3}^{0.8}$	$6.5_{0.2}^{2.5}$	$1.0_{0.3}^1$
9.71	< 5.0	< 4.3	$3.23_{0.11}^{1.3}$	$0.5_{0.2}^{0.5}$

**Notes.** The first column is the median redshift of each bin. The second and fourth columns represent the merger rate. The third and fifth ones are the specific mass accretion rate due to mergers. The label <sup>1</sup> refers to major mergers (our gold merger sample), while the label <sup>2</sup> refers to the total mergers satisfying the condition  $\text{Gini} + 0.14 \times M_{20} \geq 0.33$ .